Shack-Hartmann wavefront sensing: A new approach to time-resolved measurement of the stress intensity factor during dynamic fracture

Liuchi Li[a,*], Velat Kilic[a,b], Milad Alemohammad[a,b], Lei Yang[a], K.T. Ramesh[a,c,d], Mark A. Foster[a,b], Todd C. Hufnagel[a,c,d,*]

[a] *Hopkins Extreme Materials Institute, Johns Hopkins University, Baltimore, MD 21218, USA*
[b] *Department of Electrical and Computer Engineering, Johns Hopkins University, Baltimore, MD 21218, USA*
[c] *Department of Materials Science and Engineering, Johns Hopkins University, Baltimore, MD 21218, USA*
[d] *Department of Mechanical Engineering, Johns Hopkins University, Baltimore, MD 21218, USA*

Abstract

The stress intensity factor describes the stress state around a crack tip in a solid material and is important for understanding crack initiation and propagation. Because stresses cannot be measured directly, the characterization of the stress intensity factor relies on the measurement of deformation around a crack tip. Such measurements are challenging for dynamic fracture of brittle materials where the deformation is small and the crack tip velocity can be high. Digital gradient sensing (DGS) is capable of full-field measurement of surface deformation with a sub-micrometer sensitivity and a sub-microsecond temporal resolution, but it has only been demonstrated on centimeter-scale specimens with a spatial resolution of ~ 1 mm. This makes it challenging to measure deformations close to the crack tip. Here, we demonstrate the potential of Shack-Hartmann wavefront sensing (SHWFS), as an alternative to DGS, for measuring surface deformation during dynamic brittle fracture of millimeter-scale specimens. Using an opaque commercial glass ceramic as an example material, we demonstrate the capability of SHWFS to measure the surface slope evolution induced by a propagating crack with a micrometer spatial resolution and a sub-microsecond temporal resolution. The SHWFS apparatus has the additional advantage of being physically more compact than a typical DGS apparatus. We interpret our SHWFS measurements of the surface slope by comparing them with 2D analytical predictions and phase-field simulations as well as 3D linear-elastic FEM simulations, based on which we discuss the relevance of 3D effects around the crack tip. Then, we introduce our procedure for extracting the apparent stress intensity factor associated with the propagating crack tip using SHWFS measurements. We conclude by discussing potential future enhancements of this technique and how its compactness could enable the integration of SHWFS with other characterization techniques including x-ray phase-contrast imaging (XPCI) for multi-modal characterization of dynamic fracture.

Keywords: Dynamic fracture, Brittle material, Shack-Hartmann wavefront sensor, Surface slope measurement, Stress intensity factor, Phase-field simulation

*Corresponding author
Email addresses: lli128@jhu.edu (Liuchi Li), hufnagel@jhu.edu (Todd C. Hufnagel)

1. Introduction

The stress intensity factor (SIF or K_I in Mode-I condition) is a critical parameter for understanding the fracture of materials, and can be experimentally obtained indirectly through measurements of the displacement field in the K-dominant zone around a crack tip. An ideal measurement technique would provide full-field measurement (e.g., displacement, stress, etc) with good spatial resolution, be fast enough to allow measurement of the stress intensity around the tip of a propagating crack, and be suitable for use on an arbitrary material. Particularly challenging are studies of brittle materials, where the in-plane deformations around the crack tip can be small (on the order of tens of nanometers) and the crack-tip speed is high ($> 1\,\mathrm{km\,s^{-1}}$).

Over the past fifty years, extensive research has resulted in the development of a series of increasingly powerful optical techniques for characterizing the stress intensity of propagating cracks in a variety of materials. Notable examples include measurements relying on the photoelastic effect [1], the method of caustics [2, 3, 4], the Stress Intensity Factor Tracer [5], coherent gradient sensing (CGS) [6, 7, 8, 9]), digital image correlation (DIC) [10, 11]), the grid method [12, 13], and, most recently, digital gradient sensing (DGS) [14, 15, 16]. Any of these techniques may be effective, depending on the material under examination, the specimen geometry, and the loading conditions, but as always they all have limitations [6, 14].

Measuring the stress intensity during dynamic fracture of brittle materials (defined here as materials showing little or no plastic deformation under the loading conditions of interest) is especially challenging because the deformations around the crack tip are small, the time available for the measurement is limited by the high crack tip speeds (often in excess of $1\,\mathrm{km\,s^{-1}}$), and there is the potential for crack branching [17, 18]. One of the most powerful techniques is digital gradient sensing (DGS), which can provide accurate full-field measurements around a dynamically propagating crack tip in both transparent and opaque brittle materials [14].

When performed in reflection from an opaque material (or transparent material with a reflective coating), DGS obtains the slope associated with out-of-plane deformation due to stress concentration around the crack tip. From these displacements, the stress intensity factor can be extracted using fracture mechanics theory and the instantaneous crack velocity [19]. DGS has a demonstrated advantage over DIC [20] (and other methods measuring in-plane deformation) for measurements on highly brittle materials, in that a long optical arm (several meters) amplifies the small out-of-plane deformation and therefore enables higher detection sensitivity. DGS has been applied to studying the dynamic fracture of a variety of materials including polymers [21], oxide glasses [22], and polymer-matrix composites [23, 24]. Typical DGS implementations [20, 22, 25, 26] operate with a field of view on the order of a few centimeters, with a spatial resolution of around a millimeter[1]. In principle, DGS can be extended to operate on small specimens with a better spatial resolution, provided that small-scale speckles can be deposited onto the target plate. This can enable gaining insights into near-tip (< 1 mm) crack dynamics regarding highly brittle materials.

Here we propose a new approach (as an alternative to DGS) to measure surface profile gradients during dynamic fracture of brittle materials, based on Shack-Hartmann wavefront

[1] Here the spatial resolution means the sampling distance between two neighboring data points. In the context of DGS, this means the distance between the centroids of two adjacent subset images used for correlation. In contrast, the measurement (or detection) sensitivity is related to the size of the subset image.

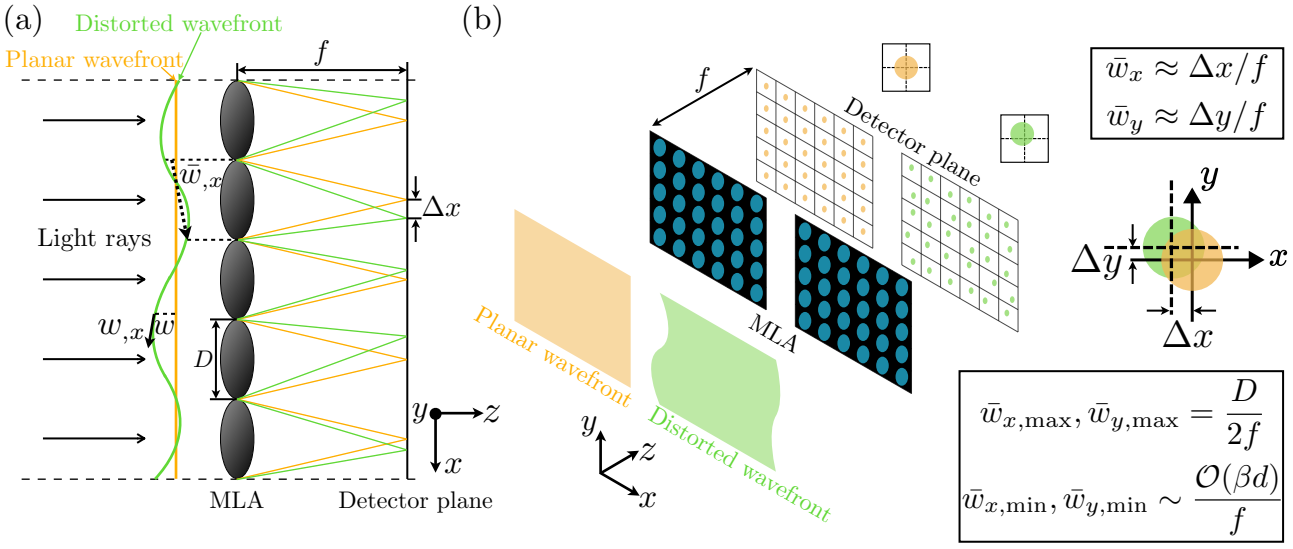

Figure 1: (a) A 2D schematic along the x direction demonstrating the working principle of SHWFS. The distorted wavefront goes through a collection of microlenses (with a uniform focal length f and a uniform pitch D), each of which performs a lens-area-averaged estimation of the wavefront's gradient, denoted as $\bar{w}_x$. (b) A 3D schematic demonstrating the working principle of SHWFS. The dynamic range ($\bar{w}_{x,\max}$, $\bar{w}_{y,\max}$) is set by $\frac{D}{2f}$ to avoid crosstalk between adjacent lenses, meaning the maximum shift $\Delta x_{\max} = \Delta y_{\max} = D/2$. The detection sensitivity ($\bar{w}_{x,\min}$ and $\bar{w}_{y,\min}$) is related to the pixel size d through a parameter β. Sub-pixel detection is possible ($\beta < 1$), provided a robust centroid detection algorithm and good signal-to-noise ratio of an SHWFS setup; see Section 2.2 for a more detailed discussion.

sensing (SHWFS) [27, 28]. Our technique retains the advantages of gradient-based methods, but it provides significantly improved spatial resolution ($\sim 10\,\mu$m) for measuring near-tip crack dynamics (< 1 mm) without the need for surface speckling while making the experimental setup more compact (with a total optical arm of < 1 m). In addition, similar to DGS, the optical arrangement of SHWFS is also flexible. This combination of high spatial resolution, physical compactness, and flexible optical arrangement, makes SHWFS ideal for multi-modal studies, particularly in combination with x-ray phase contrast imaging (XPCI) performed at synchrotron facilities [29, 30, 31]. In this paper, we describe the SHWFS technique, apparatus, and data analysis; illustrate its application to the study of dynamic fracture of a commercial glass ceramic (including extraction of the apparent stress intensity factor); and discuss potential extensions and enhancements of the technique.

2. Shack-Hartmann wavefront sensor (SHWFS)

2.1. Working principle

The Shack-Hartman wavefront sensor (SHWFS) was originally developed to measure distortions in telescope images due to atmospheric turbulence and enabled the field of adaptive optics [28]. Here we use SHWFS in a manner similar to reflection-mode DGS to measure surface slopes and extract fracture parameters during dynamic fracture. The major difference from DGS is in how the surface slope is measured. In DGS, an image of a reference pattern is recorded in reflection off of the sample; when the sample is deformed, the pattern becomes

distorted relative to the original image, and from the distortion, the surface gradients are determined. In SHWFS, instead of imaging a reference pattern, a microlens array (MLA) is used to measure distortions of a planar wavefront reflected from the sample.

A basic SHWFS consists of a micro-lens array and an image sensor, as shown in Fig. 1. With the sensor positioned at the focal plane of the MLA and illuminated by a plane wave, each micro-lens creates a focused spot on its respective optical axis. A distorted wavefront on the other hand produces a focused spot displaced from the optical axis. The displacement of the centroid of each spot is then proportional to the orientation of the wavefront averaged across the aperture of the corresponding microlens. The microlenses thus map angular deformations of the wavefront to centroid shifts at the focal plane as depicted in Fig. 1(a). Within the limit of small deformation, we have:

$$\bar{w}_x \approx \tan\bar{w}_x = \Delta x/f, \tag{2.1}$$

where $\bar{w}_x$ is the averaged gradient of the wavefront across a particular microlens, Δx is the displacement of the centroid on the detector plane, and f is the focal length of the microlens. Fig. 1(b) extends Fig. 1(a) to a 3D schematic, where we can also compute similarly the gradient in the transverse direction,

$$\bar{w}_y \approx \tan\bar{w}_y = \Delta y/f. \tag{2.2}$$

In essence, by sampling the wavefront with an MLA all of these shifts can be measured, and the whole wavefront can be reconstructed provided the scene is properly sampled both spatially and temporally [32], see section. 2.2 for a more detailed discussion.

2.2. Application in the context of dynamic fracture

We use one surface of a sample to generate a wavefront by reflecting off incoming collimated light rays. For this work, we consider only the Mode-I loading condition and use the single-notched three-point bend configuration for our experiment. As shown in Fig. 2(a), initially, when the sample is stress-free, the surface is perfectly flat, giving a planar wavefront shown as a set of equally spaced spots on the detector plane. Next, when the sample is loaded in-plane, due to Poisson's effect and heterogeneous in-plane stress distribution, the sample surface will deform out-of-plane nonuniformly, leading to non-zero surface slope and shifts of those spots on the detector plane, as shown in Fig. 2(b). During a dynamic fracture event, a propagating crack at every time instant will cause a spatial variation of the surface slope (especially near the crack tip due to stress concentration), which we calculate by first measuring the shifts Δx and Δy and next feeding into Eqns. 2.1 and 2.2. For successful detection of Δx and Δy, the following requirements should be met:

- *Spatial sampling* — The MLA pitch (the distance from the center of one lenslet to the other) should be smaller than the spatial correlation length of the distorted wavefront so that the wavefront can be safely assumed to be locally planar. Indeed, any function can be approximated locally linearly, provided it is sampled sufficiently densely. Although a smaller pitch length is preferred, we note that diffraction puts a lower bound on the pitch length for an MLA to function properly. Thus, we can think of the pitch length as similar to the correlation window size in DIC: a large window size reduces measurement

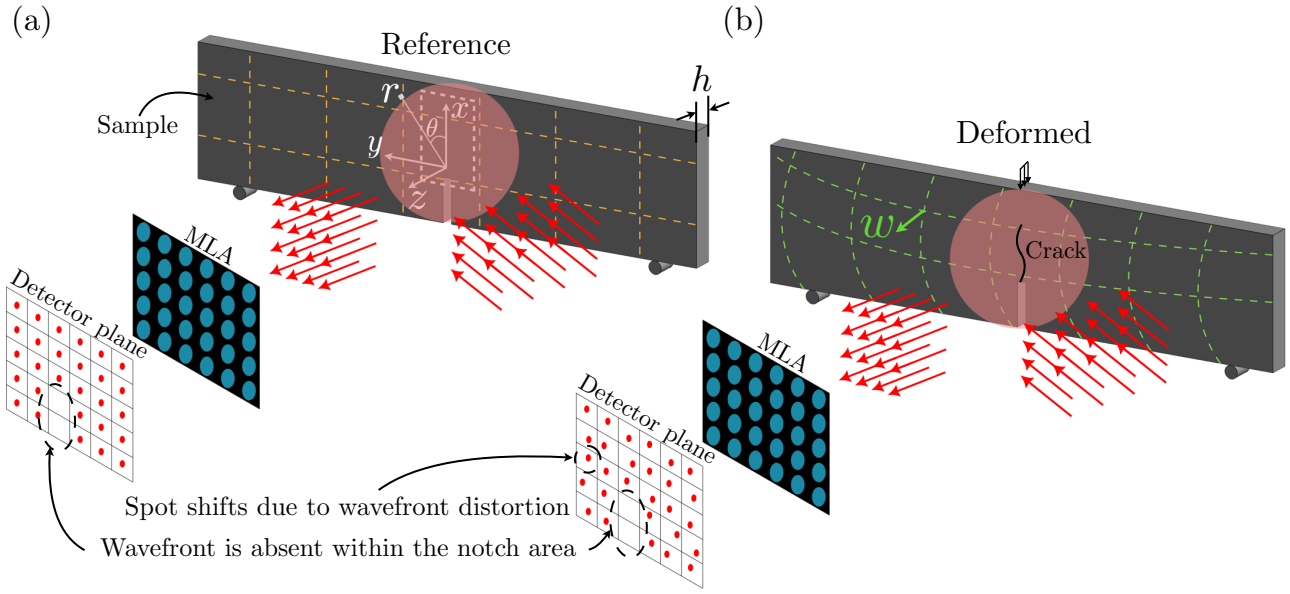

Figure 2: Application of SHWFS in the context of dynamic fracture using a single-notch three-point bending configuration. The planar (reference) wavefront is generated by the sample's smooth surface reflecting incoming collimated light rays, shown in (a). In contrast, the distorted (deformed) wavefront is caused by the surface deforming out-of-plane due to Poisson's effect, as shown in (b). In (a), the polar coordinate associated with the crack tip is also shown.

noise but is prone to averaging locally high deformation gradients, the opposite is true for a small window size. There is also a lower bound for the correlation window size with regard to accurate measurements, which is related to the average speckle feature size and contrast [33].

- *Temporal sampling* — In dynamic fracture experiments the sample surface can deform significantly and rapidly. To measure surface distortions at a given time instant, the incident wavefront must be essentially constant, which requires that it be sampled at a rate faster than its correlation time. If the incident wavefront varies significantly over a single exposure time of the recording camera, the focused spot will move as a result, and the integrated image will be blurred. The same principle also applies to DIC analysis (and any other imaging techniques), where the in-plane deformation can be viewed as the incident wavefront, whose variation should not be significant within a single exposure time of the recording camera. Therefore, a high-speed camera is needed. For imaging dynamic fracture in glass and ceramics, a frame rate on the order of one million per second is sufficient [20, 22].

- *Spot size and shape* — A tightly focused spot array on the detector plane is essential for accurate detection, and it ideally requires collimated illumination from a spatially confined source (fiber-coupled laser in our case), a smooth sample surface, and a large enough lenslet diameter. A collimated source is necessary to achieve a tightly focused spot array since the source plane is mapped onto the detector plane. A flat and smooth sample surface ensures that the in-coming planar wavefront from collimated light sources remains largely undistorted after reflection and can be detected on the camera sensor with

good contrast. However, perfect collimation, as well as perfect flatness and smoothness of the sample surface, is not a strict requirement since the spot positions are measured differentially (i.e., Δx and Δy, being referenced with respect to the positions before crack initiation). In practice, a mirror-like finish of the sample surface (with a roughness average $R_a < 0.3\,\mu\text{m}$) achieved using parallel polishing is sufficient for our purpose. Lastly, a small lenslet will lead to a large (as opposed to tightly focused) spot shape in the Fourier plane due to diffraction, which is undesired.

- *Dynamic range* — The MLA pitch (D) and focal length (f) limit the maximum surface tilt ($\bar{w}_x$ and $\bar{w}_y$) that can be measured with the current analysis algorithm. It is possible that a spot may shift so far that it moves close to the original location of a neighboring spot, causing the spot to be misidentified. This limits the range of shifts (i.e., the minimum and maximum of Δx and Δy) that can be measured with a lower bound related to the pixel size (d) and an upper bound related to the MLA pitch (D). Mathematically, $\Delta x_{\max} = \Delta y_{\max} = D/2$ (which prevents the focused spots of any two adjacent lenses from interfering with each other) and $\Delta x_{\min} = \Delta y_{\min} \sim \mathcal{O}(\beta d)$, with β depending on the signal-to-noise ratio of the setup and the centroid detection algorithm. Note that computational methods could be used to extend this range. Indeed, the centroid of each focused spot may be located with a sub-pixel resolution ($\beta < 1$) using an appropriate detection algorithm if the focused spot is spatially sampled sufficiently densely by the camera pixels and with a sufficient signal-to-noise ratio (SNR) [34].

3. Sample preparation and experimental setup

3.1. Sample preparation

We use Macor™, a commercially available glass ceramic, as an example material to test the utility of SHWFS because its mechanical properties (such as the fracture toughness K_{IC} and Young's modulus E) are well characterized and because it is highly machinable, making sample fabrication convenient. We purchased Macor™ plates (Master-Carr 8489K231) with an initial thickness of 0.0625 in (1.58 mm). We used a diamond wire saw machine to cut each plate into rectangular bars 12 mm long (along the y direction), 3 mm wide (along the x direction), and 1.58 mm thick (denoted as h in Fig. 2(a), along the z direction). We next used the same saw to create a 1 mm deep notch in each bar to produce the single-notched three-point bending configuration mentioned in the previous section. The wire used has a diameter of 250 µm, creating a notch width of 250 µm and a semicircular notch tip. We next polished one face (the x-y plane) of each bar to a mirror-like finish with diamond lapping films down to a 0.2 µm grade), using a parallel polishing machine (Allied High Tech Multiprep Polishing Machine). This forms the flat and smooth surface necessary for the SHWFS approach. After polishing, specimens are found to have a reduced thickness $h = 1.5 \pm 0.2$ mm. Note that it is not necessary to deposit a reflective coating, at least not for these specimens. For transparent materials such as glass, a reflective coating is desired.

3.2. Experimental setup

We use a custom-designed loading apparatus [31] to induce dynamic fracture under three-point bending. In this apparatus, an indenter is connected to a piezoelectric actuator (Cedrat

Technologies PPA40M), with the actuator being driven by a voltage signal that is generated by a function generator (Tektronix AFG3252) and then amplified by a high-speed voltage amplifier (PiezoDrive PD200). We place each sample over a loading plate with rolling support that sits above a vertical translation stage (OptoSigma TSD-653DMUU). We use the function generator to output a single linear voltage ramp from 0 V to 7 V over a time window of 256 µs, resulting in an indentation speed of approximately $0.13\,\mathrm{m\,s^{-1}}$. (Details of the speed measurement are provided in the appendix.) This apparatus is compact enough for operations in synchrotron facilities, and it has been used to characterize dynamic fracture of different brittle materials via XPCI [31, 35]. With this loading apparatus inducing crack propagation within a sample, we use a high-speed camera (Shimadzu HPV-X2 with a pixel size of 30 µm) to capture the distorted wavefront (subsequently $\bar{w}_x$ and $\bar{w}_y$) evolution around the propagating crack tip.

Figs. 3(a) and (b) show a schematic and a photograph of the optical setup. Illumination of the sample was provided by a pulsed laser beam (SI-LUX 640) with a fiber-coupled collimator (M92L01 and RC08FC-F01 from Thorlabs). The reflection from the sample was imaged with an infinity-corrected microscopy system (Mitutoyo 5× objective with a ThorLabs TTL200-A tube lens), a microlens array (ThorLabs MLA150-5C-M with $D = 150\,\mu\mathrm{m}$ and $f = 5.6$ mm), and a telescopic relay lens pair (ThorLabs MP105075-A) with 1.5× magnification. As with DGS, the arrangement of SHWFS optics relative to the specimen (θ in Fig. 3(a)) can be flexible, which offers free space for integrating with other image-based techniques. We also note the compactness of the experimental setup, which fits in considerably less space than typically required for DGS. This combination, namely flexible optical arrangement and physical compactness, makes SHWFS an ideal technique to work in synchrotron facilities for multi-modal fracture characterization.

A typical spot pattern from an undeformed specimen is shown in Fig. 3(c), where the field of view is approximately 1.6 mm × 1 mm, with the spacing between spots about 45 µm and an effective pixel size $d = 30/(5 \times 1.5) = 4\,\mu\mathrm{m}$. The spot spacing can be calculated using the pitch of the microlens array and the magnification ratio of the microscope and the relay: $150\,\mu\mathrm{m}/5 \times 1.5 = 45\,\mu\mathrm{m}$. We note that, from Fig. 3(c), our setup does display a small degree of pincushion distortion, which can be alleviated by optimizing the lens design. Nevertheless, the shifts (i.e., Δx and Δy), which are measured differentially, are not sensitive to such optical aberration effects. This particular setup gives $\bar{w}_{x,\max} = \bar{w}_{y,\max} \simeq 0.1$ rad and $\bar{w}_{x,\min} = \bar{w}_{y,\min} \sim 3.5 \times 10^{-4}$ rad, with the latter given by assuming a 2% of a pixel being detectable ($\beta = 0.02$) as in [22]. For our setup, sub-pixel shifts are indeed detectable (e.g., see Fig. 4(c)) as each focused spot is sampled by five to nine pixels (e.g., see Fig. 4(a)) and sub-pixel shifts can be calculated using an intensity-weighted centroid-finding algorithm [36]. Our current setup is therefore not as sensitive as a typical DGS setup which can go down to $\simeq 2.5 \times 10^{-6}$ [22]. Using a camera with a higher spatial resolution, a better sensitivity (i.e., $\sim \mathcal{O}(10^{-5})$ rad) is likely achievable. However, achieving the sensitivity of DGS ($\sim \mathcal{O}(10^{-6})$ rad) is unlikely. This is due to the fundamental tradeoff between spatial resolution (for in-plane information) and detection sensitivity (for out-of-plane information): the former scales inversely with the latter, see Eqns. 4.3 and 4.4. Nevertheless, within the near-tip region (< 1 mm) the deformation can vary with large gradients and excess $\mathcal{O}(10^{-3})$ rad [22], making attaining high spatial resolution a desired capability. Therefore, compared to DGS, our setup is particularly suitable for studying near-tip dynamics.

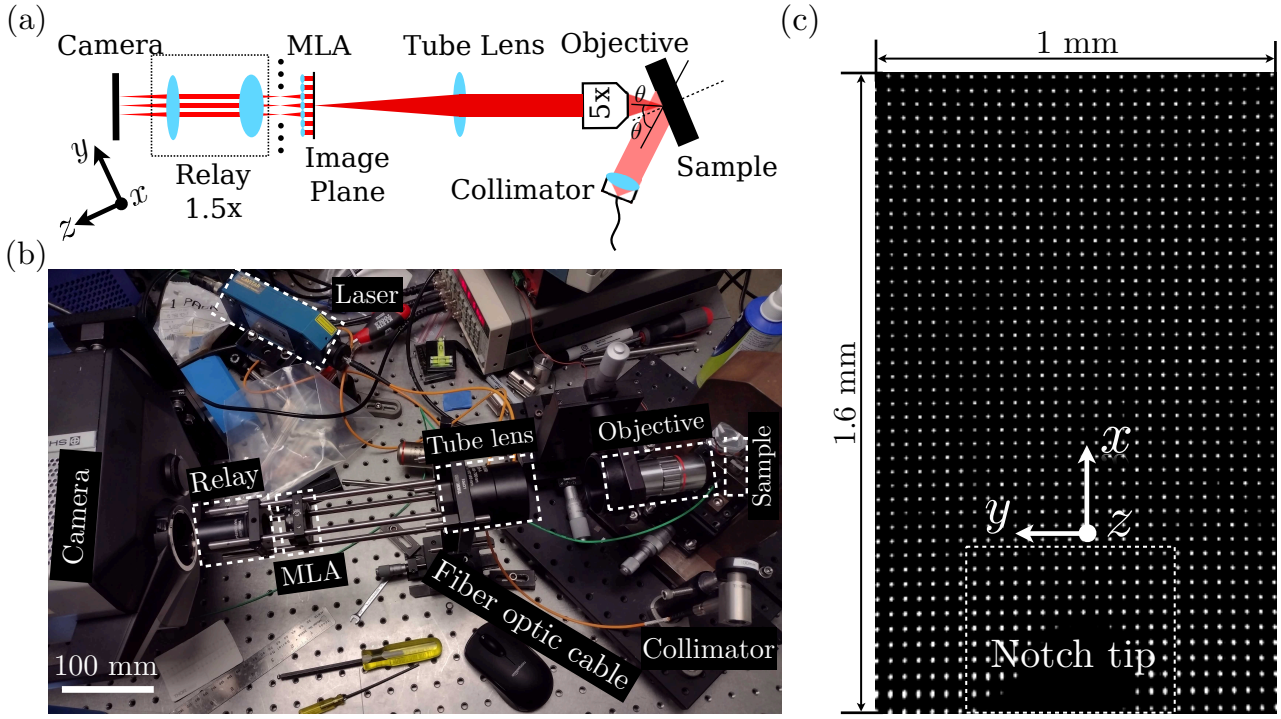

Figure 3: (a) Schematic of the SHWFS design. (b) Top-down photograph of the SHWFS setup. (c) Image formed on the camera detector showing the planar wavefront generated from the polished surface of the undeformed sample.

4. Calculation of shift and surface slope from SHWFS recording

4.1. Shift and surface slope

As a crack initiates and propagates through a sample, it will cause spots focused on the image plane to shift laterally. We measure these shifts and later use them to extract the apparent stress intensity factor (SIF). For a particular recording, we start from the initial reference image and perform a spatial partition such that each focused spot belongs to one and only one cell, as shown in Fig. 4(a). For images captured after crack initiation, we use this partition to calculate the shift Δx and Δy of each spot by finding its centroid in the reference (denoting as $[x_0, y_0]$) and the deformed configuration at a particular time instance t (denoting as $[x_t, y_t]$):

$$[\Delta x, \Delta y]|_t = [x_t - x_0, y_t - y_0]. \tag{4.1}$$

The procedure for finding the centroid of each spot is illustrated in Fig. 4. For a given spot we calculate the intensity-weighted average of all pixels that constitute that spot following Ref. [36]. Taking one spot in the reference image as an example, its centroid is given by

$$x_0 = \frac{\sum_{i,j\in S} I_{ij} \times i}{\sum_{i,j\in S} I_{ij}}, y_0 = \frac{\sum_{i,j\in S} I_{ij} \times j}{\sum_{i,j\in S} I_{ij}}, \tag{4.2}$$

where (i, j) denotes the location of a pixel, S denotes the cell captured by an individual lenslet, and I_{ij} denotes the intensity of the pixel at location (i, j). We then apply Eqn. 4.2 to find

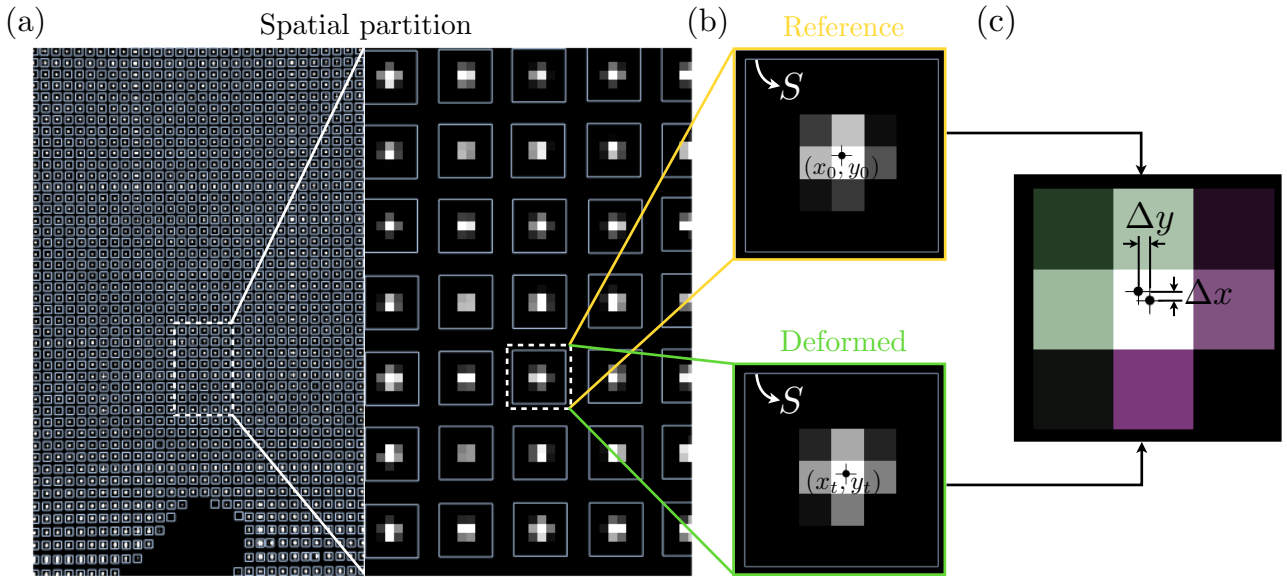

Figure 4: (a) Spatial partitioning of light spots, each assigned to a unique square cell. (b) Examples of calculating the centroid of one spot in the reference (top) and deformed (bottom) configurations. (c) An example of calculating the shifts δx and δy by overlaying the two images from (b). Areas colored in either green or purple are mismatches between the two images.

(x_t, y_t) for the same spot in each subsequent image (Fig. 4(b)). Lastly, we calculate Δx and Δy using Eqn. 4.1, as shown in Fig. 4(c).

The next step in the data reduction is converting the spot shifts (Δx and Δy) to surface slopes ($\bar{w}_x$ and $\bar{w}_y$). Care must be taken in this process because the microscope provides transverse magnification for increased spatial resolution, but this leads to angular de-magnification which in turn reduces the sensitivity to out-of-plane deformations. In Fourier optics terms, magnifying a 2D signal must necessarily reduce its spatial bandwidth. On the other hand, the relay used after the MLA images the focal plane of the MLA and increases system sensitivity to out-of-plane deformations. Putting these effects together,

$$\frac{s_r}{s_m}\bar{w}_x = \frac{d\,\Delta x}{f} \qquad \text{and} \qquad \frac{s_r}{s_m}\bar{w}_y = \frac{d\,\Delta y}{f}, \tag{4.3}$$

where s_m and s_r are the magnification factors of the microscope objective ($s_m = 5$ here) and the relay lens pair ($s_r = 1.5$ here), d is the pixel size of the camera sensor ($d = 30\,\mu\text{m}$), Δx (or Δy) is the shift in pixels, and f is the focal length of the MLA ($f = 5.6\,\text{mm}$ here). In contrast, if we want to calculate in-plane information such as the distance L between any two pixels (i_1, j_1) and (i_2, j_2), we will have:

$$s_r s_m L = d\sqrt{(i_1 - i_2)^2 + (j_1 - j_2)^2}. \tag{4.4}$$

4.2. Extraction procedure for K_I using slope data

Once we have measured the shifts Δx and Δy of each spot and computed the corresponding surface slope $\bar{w}_x$ and $\bar{w}_y$ using Eqn. 4.3, we can extract the apparent stress intensity factor K_I

by fitting the slope data to the asymptotic crack-tip stress field [37, 38] for a Mode-I crack opening under plane stress condition:

$$
\begin{aligned}
-\frac{2E}{\nu h}\bar{w}_x &= \frac{\partial\left(\hat{\sigma}_{xx}+\hat{\sigma}_{yy}\right)}{\partial x} = -\frac{1}{2}r^{-\frac{3}{2}}g(V)A_1\cos\left(\frac{3}{2}\theta\right) + \sum_{N=2}^{\infty} A_N\left(\frac{N}{2}-1\right)r^{\left(\frac{N}{2}-2\right)}\cos\left[\left(\frac{N}{2}-2\right)\theta\right], \\
-\frac{2E}{\nu h}\bar{w}_y &= \frac{\partial\left(\hat{\sigma}_{xx}+\hat{\sigma}_{yy}\right)}{\partial y} = -\frac{1}{2}r^{-\frac{3}{2}}g(V)A_1\sin\left(\frac{3}{2}\theta\right) + \sum_{N=2}^{\infty} A_N\left(\frac{N}{2}-1\right)r^{\left(\frac{N}{2}-2\right)}\sin\left[\left(\frac{N}{2}-2\right)\theta\right],
\end{aligned}
\tag{4.5}
$$

where ν, E, h are the Poisson's ratio, the Young's modulus, and the thickness of the sample, respectively; $\hat{\sigma}_{xx}$ and $\hat{\sigma}_{yy}$ are the thickness averages of stress components along the x and y directions; (r,θ) denotes the position relative to the crack-tip in polar coordinates (see Fig. 2(a)), where r at each data point can be computed following Eqn. 4.4; $A_1 = K_{\mathrm{I}}\sqrt{\frac{2}{\pi}}$ where K_{I} is the Mode-I stress intensity factor (SIF); V is the crack tip speed with $g(V)$ being a function of the instantaneous crack tip speed to account for the velocity dependency of the K-field [38]. It takes the following expression:

$$
g(V) = \frac{1+\nu}{1-\nu}\frac{\left(1-\alpha_L^2\right)\left(1+\alpha_S^2\right)}{4\alpha_L\alpha_S - \left(1+\alpha_S^2\right)^2}, \text{ with } \alpha_L^2 = 1-\frac{V^2}{C_L^2} \text{ and } \alpha_S^2 = 1-\frac{V^2}{C_S^2}, \tag{4.6}
$$

where C_L and C_S are longitudinal and shear wave speeds in the material. For relatively slow cracks ($V < 0.4C_R$ where C_R is the Rayleigh wave speed [39]), $g(V) \simeq 1$ and the velocity dependence is negligible [38]. Because our experiments are conducted within this slow crack velocity regime ($V \sim 1\times10^2\,\mathrm{m\,s^{-1}}$ while $C_R > 1\times10^3\,\mathrm{m\,s^{-1}}$), we take $g(V) = 1$. If a K-dominant field prevails around the crack tip, we may neglect higher-order terms in Eqn. 4.5 [7], arriving the following simplified expressions of Eqn. 4.5:

$$
\begin{aligned}
-\frac{2E}{\nu h}\bar{w}_x &= \frac{\partial\left(\hat{\sigma}_{xx}+\hat{\sigma}_{yy}\right)}{\partial x} \simeq -\frac{K_{\mathrm{I}}}{\sqrt{2\pi}}r^{-\frac{3}{2}}\cos\left(\frac{3}{2}\theta\right), \\
-\frac{2E}{\nu h}\bar{w}_y &= \frac{\partial\left(\hat{\sigma}_{xx}+\hat{\sigma}_{yy}\right)}{\partial y} \simeq -\frac{K_{\mathrm{I}}}{\sqrt{2\pi}}r^{-\frac{3}{2}}\sin\left(\frac{3}{2}\theta\right).
\end{aligned}
\tag{4.7}
$$

With these expressions in hand, we can determine the stress intensity (K_{I}) during crack propagation from the surface slope data using an iterative procedure. Our approach to data selection and fitting is similar to that presented in Ref. [22], and has three basic steps:

- Identify the crack tip location $\mathbf{P}$ based on the spatial distribution of $\bar{w}_x$ and $\bar{w}_y$. We use a parameter r_c to assess the uncertainty associated with $\mathbf{P}$, as shown in Figs. 5(a) and (b);

- Choose a subset of the $\bar{w}_x$ and $\bar{w}_y$ data to use in determining K_{I}. The choice is described by four parameters: $r_{\min}$, $r_{\max}$, θ_x, and θ_y. The points chosen for $\bar{w}_y$ (Fig. 5(a)) correspond to $r_{\min} \le r \le r_{\max}$ and either $\theta_y \le \theta \le \pi - \theta_y$ or $\pi + \theta_y \le \theta \le 2\pi - \theta_y$. The points chosen for $\bar{w}_x$ (Fig. 5(b)) are similar but with a different range of angles (specified by θ_x rather than θ_y). Note that the number of points chosen for $\bar{w}_y$ and $\bar{w}_x$ may be different in general.

- Fit the data from the selected points using Eqn. 4.5 to determine K_{I}. To do so, we first calculate the coefficients (denoted as b_1 and b_3) associated with the first two nonzero terms in Eqn. 4.5 (*i.e.* those with A_1 and A_3) for each data point selected from the previous step. b_1 and b_3 are determined from the geometrical location (r and θ) of each selected point. Once we have these coefficients, we perform a least-squares minimization to find the vector $\mathbf{A} = [A_1, A_3]^T$ (subsequently extracting $K_{\mathrm{I}} = \sqrt{\pi/2}A_1$), whose solution is given by the pseudo inverse of $\mathbf{B}$ shown in Fig. 4.5(c):

$$\mathbf{A}^* = \min_{\mathbf{A}} \left\| \mathbf{B}^{(y)}\mathbf{A} - \mathbf{W}^{(y)} \right\| \quad \text{or} \quad \mathbf{A}^* = \min_{\mathbf{A}} \left\| \mathbf{B}^{(x)}\mathbf{A} - \mathbf{W}^{(x)} \right\|, \tag{4.8}$$

where $\mathbf{B}^{(y)}$ (or $\mathbf{B}^{(x)}$) is a matrix containing b_1 and b_3, and $\mathbf{W}^{(y)}$ (or $\mathbf{W}^{(x)}$) is a vector containing the surface slope data for the y direction (or the x direction), as shown in Fig. 5(c). Alternatively, we can merge the two minimization problems into one: $\mathbf{A}^* = \min_{\mathbf{A}} \left\| [\mathbf{B}^{(y)}; \mathbf{B}^{(x)}]\mathbf{A} - [\mathbf{W}^{(y)}; \mathbf{W}^{(x)}] \right\|$. Certainly, more higher-order terms from Eqn. 4.5 can be included in the fitting process [7]. Note that as long as the number of terms is smaller than the number of data points, the minimization problem (Eqn. 4.8) remains over-deterministic (i.e., the matrix $\mathbf{B}$ remains "tall".). We further regularize Eqn. 4.8 as the following:

$$\mathbf{A}^* = \min_{\mathbf{A}} \left\| \hat{\mathbf{B}}^{(y)}\mathbf{A} - \hat{\mathbf{W}}^{(y)} \right\| \quad \text{or} \quad \mathbf{A}^* = \min_{\mathbf{A}} \left\| \hat{\mathbf{B}}^{(x)}\mathbf{A} - \hat{\mathbf{W}}^{(x)} \right\|, \tag{4.9}$$

where $\hat{\mathbf{B}}(i,:) = c_i\mathbf{B}(i,:)$ and $\hat{\mathbf{W}}(i) = c_i\mathbf{W}(i)$, for both (x) and (y), with $c_i = \frac{M}{r_i \sum_{k=1}^{k=M} \frac{1}{r_k}}$. Above, for either $\bar{w}_x$ or $\bar{w}_y$, i denotes one data point and r_i is its corresponding distance to the crack tip. Effectively, by using Eqn. 4.9 we weigh observations from different distances to the crack tip equally. This is because the number of data points at a given distance is proportional to r, so this procedure ensures that all distances are weighted equally in the fit; without, the fitting would over-emphasize points away from the crack tip. This fitting procedure using the out-of-plane information is similar to that which uses in-plane information (such as from DIC measurements) to extract K_{I} for polymers [11].

As we can see from Eqn. 4.5 the terms dominating the solution of Eqn. 4.8 are those from points close to the crack tip, which have large $r^{-3/2}$ and $r^{-1/2}$ as well as large $\bar{w}_x$ and $\bar{w}_y$. This makes precise determination of the position of the crack tip ($\mathbf{P}$) critical. On the other hand, we want to exclude data that are too close to the crack tip and near the crack path, because the SHWFS measurements become unreliable there due to the highly localized deformation and discontinuity. Thus, selecting an appropriate value of $r_{\min}$ balancing these considerations is also important. The other parameters ($r_{\max}$, θ_x, and θ_y) are much less important than $\mathbf{P}$ and $r_{\min}$.

In practice, we have found that choosing $r_{\min} = 20$ pixels (0.08 mm on the specimen), which excludes data from the closest two or three spots to the crack tip, works well with our setup. Other parameters chosen are $r_{\max} = 110$ pixels (equivalent to 0.4 mm on the sample, which covers essentially the whole horizontal field of view), $\theta_y = \pi/6$, and $\theta_x = \pi/4$. Lastly, we locate $\mathbf{P}$ for each snapshot based on the symmetric spatial pattern of w_y and w_x shown in Fig. 6(a) and Fig. 7(a), in a way similar to Ref. [16]. We denote this location of $\mathbf{P}$ as the base position,

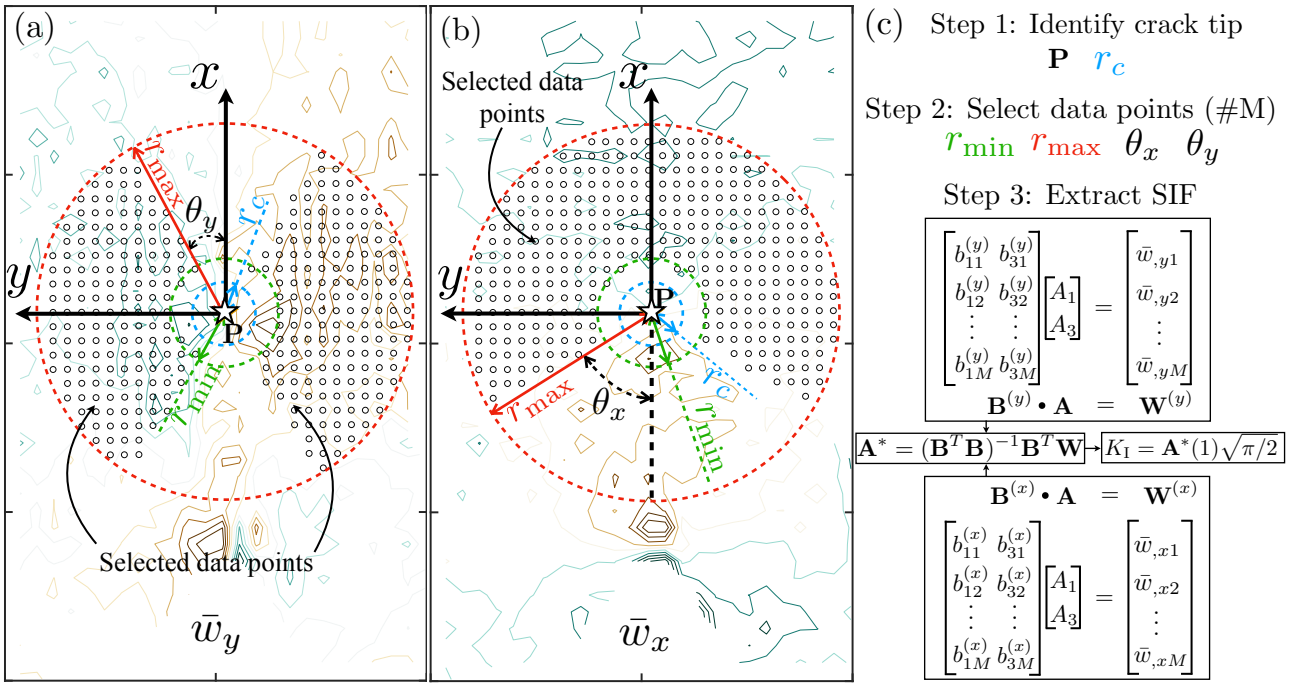

Figure 5: Selection of points for determining K_{I} from surface slope data. The background of parts (a) and (b) show contour plots of $\bar{w}_y$ and $\bar{w}_x$, respectively (see 5.1 for a description of these data). The superimposed circles represent positions from which the surface slope data were used to determine K_{I}. The region of data used is specified by four parameters: the position of the crack tip, $\mathbf{P}$; inner and outer radii, $r_{\min}$ and $r_{\max}$; and the half-angle of an excluded region, θ_y and θ_x. The parameter r_c reflects uncertainty in determining $\mathbf{P}$, as described in the text. (c) A flow chart showing steps for calculating the apparent stress intensity factor K_{I}.

whose location is indicated by the star colored in white with a black border line in Figs. 5(a) and (b).

Of course, there is uncertainty associated with both $\mathbf{P}$ and $r_{\min}$, especially the former, and it is important to quantify how this affects the value K_{I} determined from the measurements. We assess the uncertainty in $\mathbf{P}$ by sampling multiple positions of $\mathbf{P}$ in a circle of a radius of r_c centered at the base position of $\mathbf{P}$. Similarly, we apply a variation r_d to the value of $r_{\min}$. We calculate the value of K_{I} over each of these ranges and report the average value. We used $r_c = r_d = 5$ pixels (0.02 mm) in this work, and find that this choice produces reasonable results. Finally, we do not analyze data from the initial ten images starting from crack initiation (i.e., crack lengths less than 0.3 mm) due to the difficulty in identifying $\mathbf{P}$ for such short cracks. We note that this could be alleviated by using fatigue-precracked specimens, where the more pronounced stress concentration would aid in the determination of $\mathbf{P}$.

5. Results

5.1. Measurement of surface slope $\bar{w}_x$ and $\bar{w}_y$

Fig. 6(a) shows the distribution of $\bar{w}_y$ across the field of view at three instants during a representative dynamic fracture experiment from a notched three-point bend sample of Macor™. We use the crack initiation time as a reference ($t = 0$). For this experiment with images collected at 5 Mfps, the time between frames is 0.2 µs. As a comparison, we calculate the plane-stress

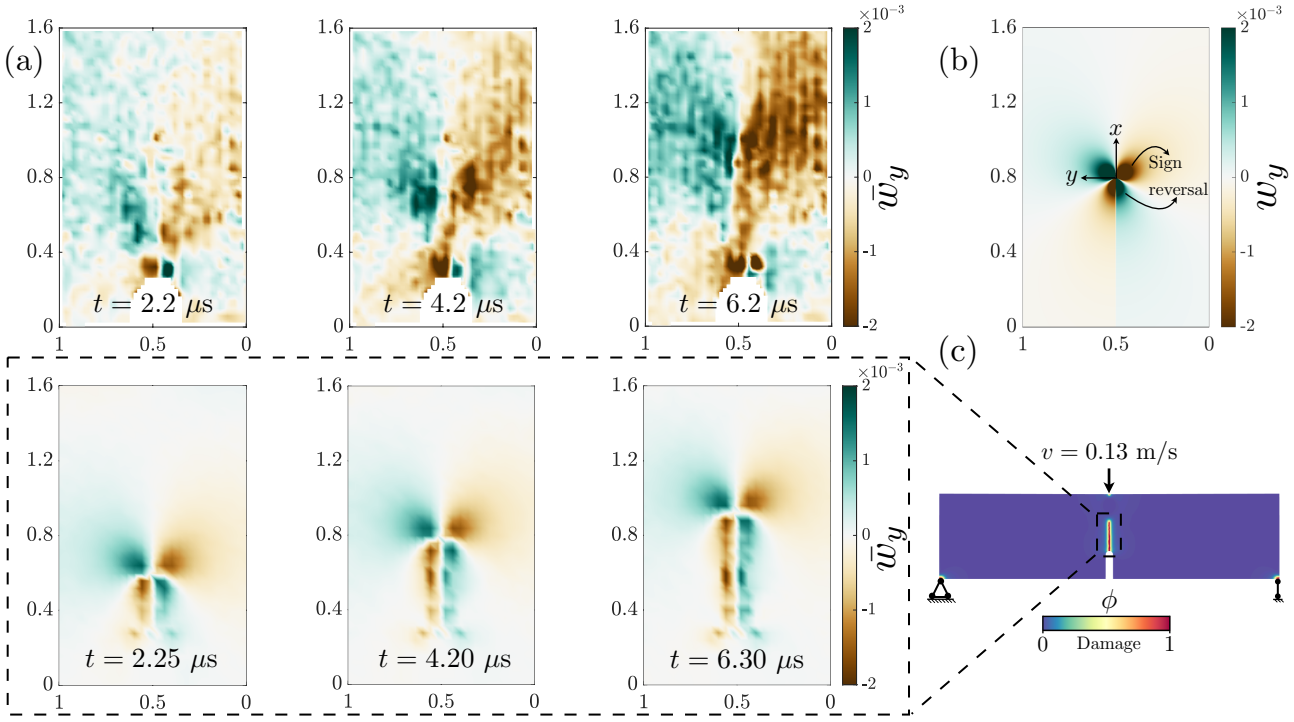

Figure 6: (a) Spatial distribution of surface slope $\bar{w}_y$ determined from SHWFS measurements at three different times after crack initiation ($t = 0$). (b) Spatial distribution of w_y calculated from the near-tip stress field (analytical solution) using a sample thickness $h = 1.5\,\text{mm}$, given a crack tip at the center of the image. (c) A schematic showing the dynamic phase-field simulation and three plots showing the computed distribution of $\bar{w}_y$ at times comparable to the experimental data in (a). The unit for all color bars is radians, and that for all axes is millimeters.

analytical prediction of w_y (Fig. 6(b)) using Eqn. 4.7 and the mechanical properties of Macor™ ($E = 66.9\,\text{GPa}$, $\nu = 0.29$, and $K_{\text{IC}} = 1.53\,\text{MPa}\,\text{m}^{1/2}$) [40], as well as the sample thickness h = 1.5 mm. As an additional comparison we compute $\bar{w}_y$ (Fig. 6(c)) from dynamic phase-field simulations [41, 42] of fracture using a custom code [43]. (Details of the phase-filed simulations are provided in the Appendix). This computation is achieved by plugging in the in-plane stresses σ_{xx} and σ_{yy} obtained from the simulation into Eqn. 4.7, in which the mechanical properties of Macor™ and a sample thickness $h = 1.5\,\text{mm}$ is used. We believe that the highly localized surface slope profile in the simulation results in the wake of the crack is an artifact of the phase-field algorithm, which smears the sharp crack over a certain region, in which the stress does not completely drop to zero.

The analytical predictions and PF simulation results are consistent with each other in terms of the spatial distribution of $\bar{w}_y$. However, the agreement with the SHWFS measurements is not as good. Although the pattern of $\overline{w}_y$ from SHWFS is broadly similar to that from the analytical and numerical calculations, there are quantitative differences. In particular, for longer crack lengths the measured gradients are more spread out than the calculated gradients. A similar observation can be made for $\bar{w}_x$ by comparing Fig. 7(a) (SHWFS measurements) with Figs. 7(b) and (c) (analytical and numerical results). In addition, the sign reversal of $\bar{w}_y$ in the wake of the crack, shown in calculations (Fig. 6(b)), is not captured well in the measurement.

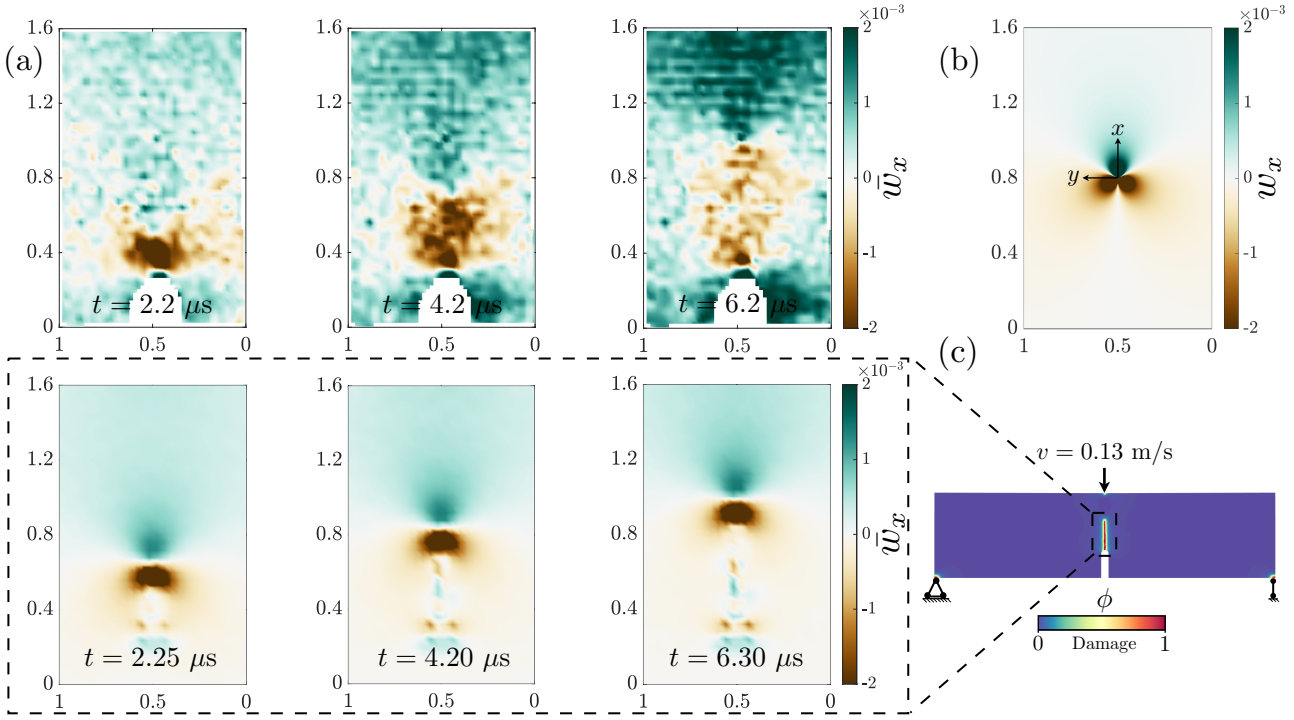

Figure 7: Similar to Fig. 6 but for surface slopes w_x. (a) Spatial distribution of $\bar{w}_x$ determined from SHWFS measurements. (b) Analytical solution for the spatial distribution of w_x, calculated using a sample thickness $h = 1.5$ mm. (c) A schematic showing the dynamic phase-field simulation and three plots showing the computed distribution of $\bar{w}_x$. The unit for all color bars is radians, and that for all axes is millimeters.

For both $\bar{w}_y$ and $\bar{w}_x$, the major difference between experiments and analytical (and numerical) calculations is the sample thickness: the former is 3D, while the latter is deduced from a 2D plane stress condition which only applies when the sample thickness is small compared to the in-plane dimensions. (We rule out the possibility of significant plastic deformation around the crack tip being responsible for the disagreement because the material behaves in a brittle manner under these conditions.) In our experiments, the sample has a thickness $h = 1.5$ mm, which is on the same order of magnitude as the sample height (3 mm). This raises the question of whether a plane stress condition is a good approximation to the stress state, especially near the crack tip (or rather, the crack front). Indeed, previous studies [44, 7] have pointed out the importance of 3D effects, and in particular that the out-of-plane stress (σ_{zz}) may not be negligible near the crack tip. The significance of this is that, if 3D effects are important, a calculation of the stress intensity (K_{I}) based on an assumption of a 2D stress state (as we do here) will be smaller than that from a true 2D stress state. Because K_{I} is calculated from the surface slope data, we suspect that this kind of 3D effect is also responsible for differences between the measured surface slope and those calculated analytically and numerically from phase-field simulations. We consider this in detail in the next section.

5.2. 3D effects around the crack tip for deviating surface slope profile from analytical predictions

To check the potential relevance of 3D effects on altering the distribution of $\bar{w}_y$ and $\bar{w}_x$, we performed full-scale 3D FEM calculations using Abaqus/Explicit. From these calculations,

we can directly get the out-of-plane displacement w and then calculate $\bar{w}_y$ and $\bar{w}_x$. For our purpose, it suffices to consider only the linear elastic response of the sample without fracture. We construct two single-notched three-point bending models (see Appendix for details). The specimen in both models have the same height (3 mm) and length (12 mm) as the specimens used in the experiment, but one has a thickness of 0.15 mm (referred hereafter as the thin sample, where plane stress should be valid) and the other has a thickness of 1.5 mm (referred hereafter as the thick sample, same as in experiments). We create a sharp crack with a length of 1 mm for both samples. We impose a load of F to the thin sample and a load of $10F$ to the thick sample via a standard three-point flexural test setup. Scaling the load with the sample thickness keeps in-plane stress gradient nominally the same for the two models (see Appendix). This allows us to directly examine the role of 3D effects: if they are not prominent (*i.e.* plane stress being a good approximation), similar in-plane stress gradients should give rise to similar surface slopes. In other words, the spatial distribution of $\bar{w}_y$ and $\bar{w}_x$ should directly scale with the sample thickness provided the in-plane stress gradient remains unchanged and a plane-stress condition is satisfied, as suggested by Eqn. 4.5. Otherwise, 3D effects are nonnegligible. In practice, we tune F until the surface slope distribution of the thin sample shows a similar pattern to that obtained from the plane-stress analytical prediction. We then take the calibrated F to calculate the surface slope profile of the thick sample (using a load of $10F$).

Fig. 8 shows analytical calculations as well as Abaqus simulation results. Again, a plane-stress condition implies that both $\bar{w}_y$ and $\bar{w}_x$ for the thick sample should simply be 10 times those of the thin sample, in a way similar to the comparison between Fig. 8(a) and Fig. 8(c) and the comparison between Fig. 8(e) and Fig. 8(g). However, this is not what we see from Abaqus simulations by comparing Fig. 8(b) to Fig. 8(d) and Fig. 8(f) to Fig. 8(h).

In particular, the spatial distribution of both $\bar{w}_y$ and $\bar{w}_x$ from the thick sample is more spread out than that of the thin sample, with the former resembling more closely the SHWFS measurements and the latter resembling more closely the 2D plane-stress analytical results. Also, the sign reversal of $\bar{w}_y$ in the wake of the crack, predicted by a plane-stress analytical solution (as shown in Figs. 8(a) and (c)), is much less pronounced when the sample is thick (by comparing Fig. 8(d) to Fig. 8(b)). This could explain why in our experiments the sign reversal of $\bar{w}_y$ was not well captured. Due to such nonnegligible 3D effects, the surface slope distribution of the thick sample takes a considerable contribution arising from the out-of-plane stress σ_{zz} (see Appendix for an explicit calculation of σ_{zz} from the 3D FEM models).

5.3. Extraction of K_I

Although 3D effects are important for this particular specimen geometry, we can extract an approximate stress intensity factor (K_I) on the basis of the 2D approximation in Eqn. 4.5. Figure 9(a) shows how K_I varies as a function of the apparent crack length. To determine K_I we use the first two terms in Eqn. 4.5 in fitting to the data following Eqn. 4.9. Additional terms can be included but we find that they have little effect on the value of K_I (see Appendix for a plot). Note that the average crack speed is about 150 m/s ($< 0.1C_R$), which is in the "slow" crack regime.

We observe that K_I fluctuates around a mean value of $0.8\,\mathrm{MPa\,m^{1/2}}$ as the apparent crack length extends from 0.3 mm to 1.2 mm. This value is somewhat lower than the static fracture toughness of Macor™, $K_\mathrm{IC} = 1.53\,\mathrm{MPa\,m^{1/2}}$ [40]. Other researchers have observed apparent

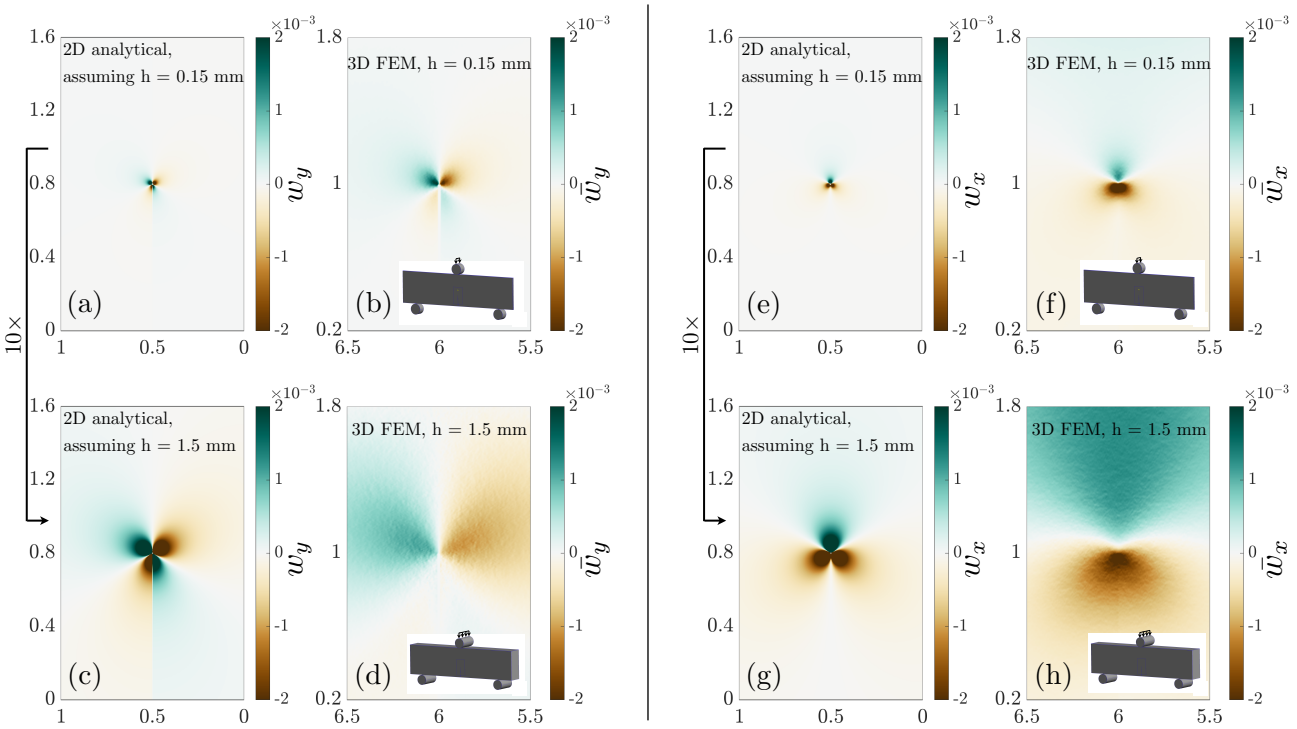

Figure 8: Left column: spatial distribution of $\bar{w}_y$ calculated from the 2D analytical solution (Eqn. 4.5 using $K_{\mathrm{IC}} = 1.53\,\mathrm{MPa\,m^{1/2}}$) and the 3D FEM simulation for the thin sample (a) and (b), and for the thick sample (c) and (d). Right column: spatial distribution of $\bar{w}_x$ calculated from the 2D analytical solution (Eqn. 4.5 using $K_{\mathrm{IC}} = 1.53\,\mathrm{MPa\,m^{1/2}}$) and the 3D FEM simulation for the thin sample (e) and (f), and for the thick sample (g) and (h).

dynamic fracture toughnesses that are lower than the corresponding static fracture toughness (or critical stress intensity factor) in a variety of materials (such as Homalite-100 [17, 45] and soda-lime glass [22, 16]).

The exact causes for the difference in static and dynamic fracture toughnesses are not well understood, but these include thickness-dependent 3D effects around the crack tip [44, 7] and the lack of K-dominance during dynamic fracture [3].

6. Summary and outlook

In this work, we demonstrate a new approach for estimating the apparent stress intensity factor (K_{I}) during dynamic fracture of brittle solids by measuring the surface slope profile using a Shack-Hartmann wavefront sensor (SHWFS). We have successfully measured the surface slope ($\bar{w}_y$ and $\bar{w}_x$) evolution during the fracture of millimeter-scale Macor™ samples with a spatial resolution of 45 µm and a temporal resolution of 0.2 µs. We observe that the distributions of $\bar{w}_y$ and $\bar{w}_x$ measured from SHWFS differ from those predicted by plane stress analytical solutions and phase-field simulations. Using full-scale 3D FEM analysis of the sample geometries we have shown that the differences can be explained by the existence of 3D effects. We observe that the effective fracture toughness computed from the SHWFS measurements, assuming a 2D state, is less than the static fracture toughness K_{IC}.

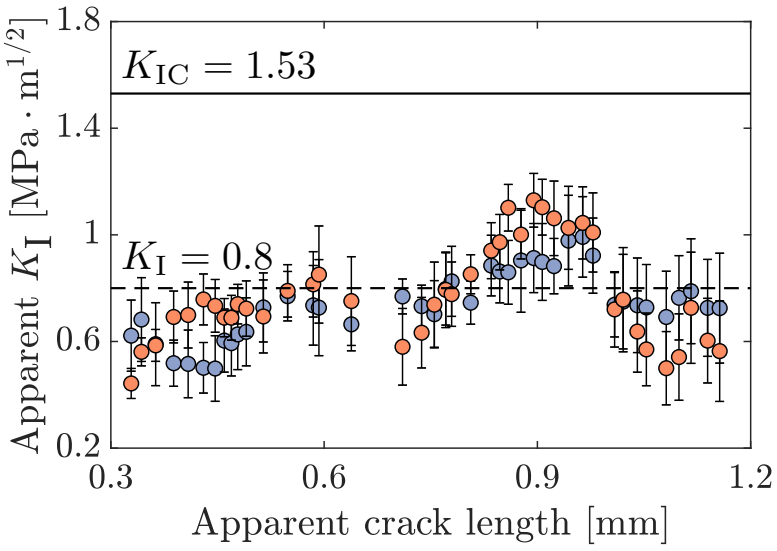

Figure 9: Evolution of the apparent stress intensity factor K_I as a function of the apparent crack length, using both the $\bar{w}_y$ data (blue circles) and the $\bar{w}_x$ data (red circles). The error bar associated with each data point indicates the scatter coming from varying $\mathbf{P}$ and $r_{\min}$. The black solid line indicates the static fracture toughness $K_{IC} = 1.53\,\mathrm{MPa\,m^{1/2}}$, while the black dashed line indicates the average apparent stress intensity factor with a value of $0.8\,\mathrm{MPa\,m^{1/2}}$.

Although we have only demonstrated applying SHWFS in the "slow" crack regime, there is no practical barrier to applying it in the "fast" crack regime (crack speed > 1 km/s). This is because we directly image the specular reflection of a laser beam off the surface of the specimen, resulting in excellent signal-to-noise ratio. The major practical limitations are associated with the framing rate of the camera, and the field of view possible with the given optics.

Compared to a typical DGS apparatus, the SHWFS apparatus has improved spatial resolution while requiring less physical space to implement. As such, SHWFS can be especially useful for small-scale fracture experiments and is ideal for multi-modal studies, particularly in combination with x-ray phase contrast imaging (XPCI) performed at synchrotron facilities. One potential application in this regard is studying the dynamic fracture of materials under high-rate loadings using miniaturized desktop Kolsky bar setups [46] at synchrotron facilities [31]. In addition, unlike DIC, SHWFS does not require the preparation of speckle patterns on specimens (which is particularly challenging for small-scale experiments), and it can be used on any material so long as the surface can be polished to a mirror-like finish. The setup of SHWFS can also be modified to study transparent materials without the need for coating a specimen's sample to be reflective, in a way similar to transmission-mode DGS [14]. As such, the flexibility of SHWFS with regard to sample preparation also makes it adaptable to studying a broad range of brittle materials. We discuss two directions for improvement:

- Increasing the resolution of the measurement. There are two aspects in this direction: increasing the smallest detectable deformation (i.e., sensitivity) and increasing the spatial resolution of detection. The smallest detectable deformation is related to the shift of the reflected spots on the camera sensor. Given a fixed field of view determined by the microscope objective, the shift is tied to the focal length (denoted as f) of the multi-lens array (MLA), with a larger focal length producing a larger shift (Eqn. 2.1 and 2.2). The

spatial resolution is tied to the pitch of the MLA (denoted as D, essentially how large each microlens is). Since each microlens performs an average measurement of surface slope across its area, we will want an MLA with a small pitch (i.e., a smaller microlens) to increase the spatial resolution. However, diffraction effects limit the smallest pitch and the largest focal length of an MLA. Therefore, a tradeoff exists between a small D and a large f. Specifically, the Fresnel number $\frac{D^2}{f\lambda}$ must be larger than unity where λ is the wavelength. Our current setup ($D = 150\,\mu\text{m}$, $\lambda = 640$ nm, and $L = 5.6$ mm) leads to a Fresnel number of about 6.2. Choosing a different MLA for our setup may lead to a better detection sensitivity with minimal sacrifice to the spatial resolution or vice versa. Nevertheless, it is important to note that the choice of MLA is application-specific: depending on the specific experiment details (such as material type and size), a different MLA may be needed for the desired detection sensitivity and spatial resolution. Lastly, note that we also have the option of enlarging the field of view (by using a microscope objective with a smaller magnification, see Eqn. 4.3), but this can require a larger sample and lead to a change of the loading apparatus.

- Increasing the accuracy of the crack tip position determination. We have shown that an accurate estimation of K_{I} depends heavily on accurately identifying the crack tip location (as also highlighted in [47, 48]). This is quite challenging to do at the millimeter scale based solely on the distribution pattern of the surface slope, especially given the presence of noise in experimental measurements. In this regard, one possibility is exploiting the distribution property of the out-of-plane asymptotic field, in a way that extends the novel approach proposed by [48] which takes advantage of the separability of the in-plane asymptotic field (e.g., the in-plane displacement field measured by DIC). Another possibility is integrating SHWFS and x-ray phase contrast imaging (XPCI), with the latter providing more accurate time-resolved identification of the crack tip location. In XPCI, phase perturbation introduced by the sample is exploited to modulate the intensity recorded at the image detector plane [49]. Since the surface of a crack induces a steep phase gradient, a phase-contrast image can have a significantly enhanced contrast compared to conventional radiography. XPCI has already been used to characterize the crack dynamics within different brittle materials from ceramics [31] to glass [30, 35] taking advantage of spatially-coherent high-energy X-rays provided by synchrotron facilities.

7. CRediT Authorship Contribution Statement

L. Li. Conceptualization, Methodology, Experiment, Numerical Simulation, Formal Analysis, Investigation, Visualization, Writing – Original & Draft. **V. Kilic**. Methodology, Experiment, Formal Analysis, Investigation, Visualization, Writing – Original & Draft. **M. Alemohammad**. Methodology, Experiment, Writing – Review & Editing. **L. Yang**. 3D FEM simulations, Writing – Review & Editing. **KT Ramesh**. Conceptualization, Resources, Supervision, Funding Acquisition, Project Administration, Writing – Review & Editing. **MA Foster**. Conceptualization, Methodology, Resources, Supervision, Project Administration, Writing – Review & Editing. **TC Hufnagel**. Conceptualization, Resources, Supervision, Funding acquisition, Project Administration, Writing – Review & Editing.

8. Acknowledgements

We thank Dr. Jason Harris, Dr. Charlene Smith, and Dr. Xinyi Xu from Corning Inc. for stimulating discussions on glass ceramics, as well as Nand Vommi for his help with sample preparation, Justin Moreno and Matthew Shaeffer for their assistance to our experiments, and Dr. Chengyun Miao for insightful discussions on DGS. We are also thankful for the constructive comments from reviewers that helped us improve our manuscript. We gratefully acknowledge financial support provided by the Corning Research and Development Corporation. The project was sponsored in part by the Department of Defense, Defense Threat Reduction Agency under the Materials Science in Extreme Environments University Research Alliance, HDTRA1-20-2-0001. The content of the information does not necessarily reflect the position or the policy of the federal government, and no official endorsement should be inferred.

Appendix A. Measuring the indentation speed

We recourse to image analysis to measure the indentation speed of the piezo actuator (which drives the indenter), following the same procedure the lead author has used to measure the angle of repose of granular materials [50]. We record the motion of the bottom edge of the piezo actuator using a high-speed camera, shown in Fig. A.10(a), and we compute the position variation, shown in Fig. A.10(b) as a function of time by binarizing each image and finding the boundary of the actuator in each image. From the position data, we can calculate the instantaneous velocity, shown in Fig. A.10(c), using a finite-difference scheme. We see that the velocity is fairly constant. We calculate the average velocity of the actuator following the above procedure, both with and without indenting a sample. Fig. A.10(d) shows the result. In short, the indentation velocity stays largely unchanged, equaling around 0.13 m/s regardless of whether indenting a sample or not.

Appendix B. Variational phase-field approach to fracture

The variational phase-field method to fracture [51] uses a scalar field $\phi \in [0, 1]$ to describe the spatial distribution of damage ($\phi = 0$ being intact and $\phi = 1$ being completely damaged) of a simulation domain through a length scale parameter ℓ. Consequently, a crack (a sharp interface) is smeared through a smooth variation of ϕ over ℓ. The parameter ℓ represents active mechanisms in the process zone, determining the threshold for crack nucleation [51]. Essentially, to model a dynamic fracture problem, we want to minimize the following incremental Lagrange energy functional $\mathbf{I}_\ell$ by the principle of least action [42]:

$$\mathbf{I}_\ell(u, \dot{u}, \phi) = \int_{t_1}^{t_2} \left\{ \int_\Omega \left[\frac{\rho}{2} |\dot{u}|^2 - \mathcal{W}^e(u, \phi) - G_{\mathrm{C}} \gamma_\ell(\phi, \nabla\phi) + \rho b \cdot u \right] \mathrm{d}\Omega + \int_{\partial\Omega} t \cdot u \mathrm{dS} \right\} \mathrm{dt}, \quad \text{(B.1)}$$

under the constraint $\dot{\phi} > 0$ to account for the irreversibility of a fracture process. Above, u is the displacement field, with $\dot{u} = \frac{\partial u}{\partial t}$ the velocity field, ρ the material density, ϕ the phase field parameter indicating the degree of material damage, $\mathcal{W}^e$ the elastic strain energy density, G_{C} the critical energy release rate (or fracture toughness) [52], γ_ℓ the (regularized) fracture energy density, b the gravitational constant, and t the surface traction. We follow [41] for modeling

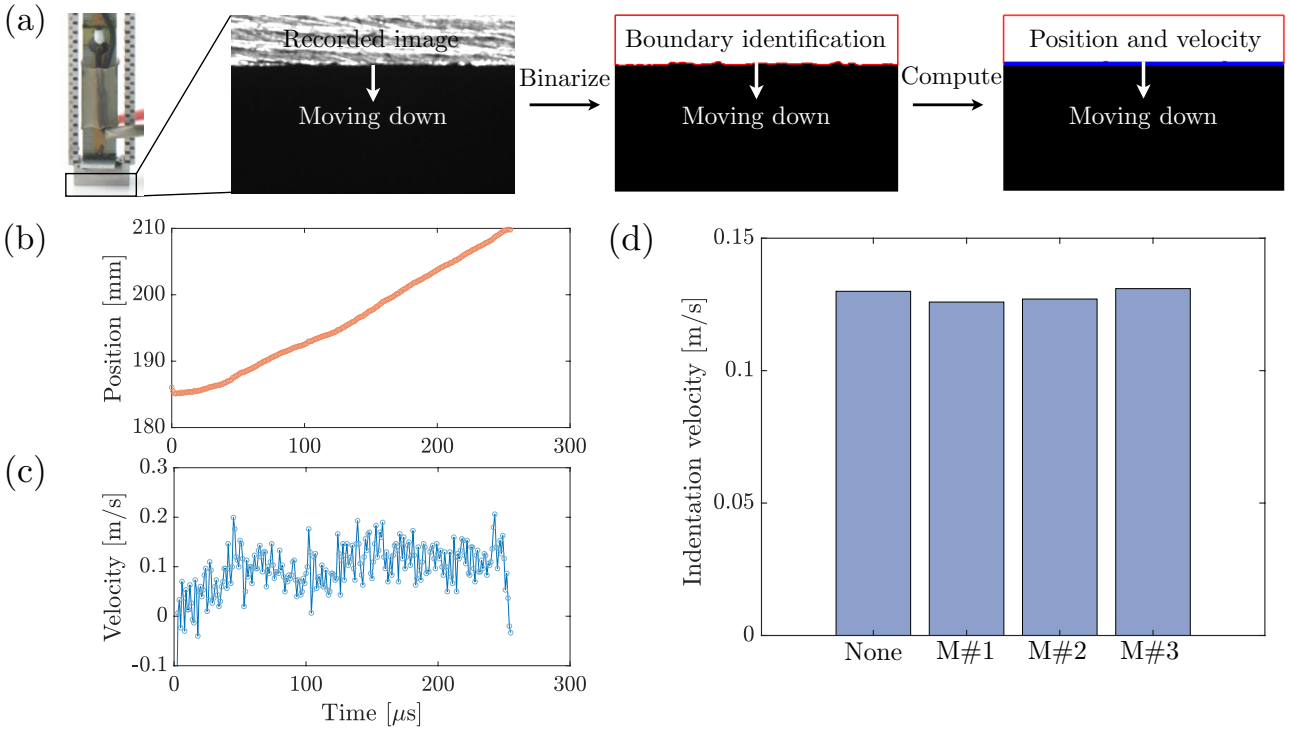

Figure A.10: (a)A schematic showing the steps of calculating the indentation speed. (b) The position evolution of the actuator's bottom edge as a function of time without indenting a sample. (c) The corresponding speed evolution of the actuator's bottom edge as a function of time. (d) The time-averaged indentation speed without and with indenting a sample (which is repeated three times).

brittle solids, decomposing the elastic strain energy shown in Eqn. B.1 to a tensile part ("+") and a compressive part ("$-$"), with the phase-field acting only on the former:

$$\mathcal{W}^e(\epsilon_{ij},\phi) = [(1-k)(1-\phi)^2 + k]\mathcal{W}^{e,+}(\epsilon_{ij}) + \mathcal{W}^{e,-}(\epsilon_{ij}), \tag{B.2}$$

where ϵ^d is the d-th eigenvalue of ϵ, n^d is the corresponding eigenvector, $\langle x\rangle_+$ stands for $(x+|x|)/2$, and $\langle x\rangle_-$ stands for $(x-|x|)/2$ with $|x|$ being the absolute value of x. We can then express $\mathcal{W}^{e,+}(\epsilon_{ij})$ and $\mathcal{W}^{e,-}(\epsilon_{ij})$ as the following:

$$\mathcal{W}^{e,+}(\epsilon_{ij}) = \frac{1}{2}\lambda\langle\epsilon_{kk}\rangle_+^2 + \mu\epsilon_{kj}^+\epsilon_{jl}^+\delta_{kl}, \tag{B.3}$$

$$\mathcal{W}^{e,-}(\epsilon_{ij}) = \frac{1}{2}\lambda\langle\epsilon_{kk}\rangle_-^2 + \mu\epsilon_{kj}^-\epsilon_{jl}^-\delta_{kl}, \tag{B.4}$$

where λ and μ are the Lamé constants that can be determined from the Young's modulus E and the Poisson's ratio ν. The (regularized) fracture energy density γ_ℓ takes the following form:

$$\gamma_\ell = \frac{1}{4c_w\ell}\left(w(\phi) + \ell^2|\nabla\phi|^2\right), \text{with } c_w = \frac{1}{2} \text{ which implies } w(\phi) = \phi^2. \tag{B.5}$$

Applying the principle of least action to Eqn. B.1 with $\mathcal{W}^e$ and γ_ℓ expressed by Eqns. B.2, B.3, B.3, and B.5, we arrive at the following two governing equations:

$$\sigma_{ij,j} + b_i = \rho \ddot{u}_i, \tag{B.6}$$

$$\left[1 + \frac{4c_w \ell (1-k)}{G_{\mathrm{C}}} \mathcal{W}^{e,+}\right] \phi - \ell^2 \phi_{,ii} = \frac{4c_w \ell (1-k)}{G_{\mathrm{C}}} \mathcal{W}^{e,+}, \tag{B.7}$$

where $\sigma_{ij} = \partial \mathcal{W}^e / \partial \epsilon_{ij}$. We enforce the irreversible growth condition $\dot{\phi} > 0$ using a strain-history field [41] over the simulation domain:

$$\mathcal{H}(x,t) = \max_{s \in [0,t]} \mathcal{W}^{e,+}\left(\epsilon(x,s)\right) \;\; \forall\, x \in \Omega. \tag{B.8}$$

Replacing $\mathcal{W}^{e,+}$ with $\mathcal{H}(x,t)$ in Eqn. B.7 we then want to solve:

$$\sigma_{ij,j} + b_i = \rho \ddot{u}_i, \tag{B.9}$$

$$\left[1 + \frac{4c_w \ell (1-k)}{G_{\mathrm{C}}} \mathcal{H}\right] \phi - \ell^2 \phi_{,ii} = \frac{4c_w \ell (1-k)}{G_{\mathrm{C}}} \mathcal{H}, \tag{B.10}$$

together with the following Neumann boundary conditions (plus any existing Dirichlet boundary conditions) :

$$\sigma_{ij} n_j = t_i \text{ on } \partial\Omega, \tag{B.11}$$

$$\phi_{,i} n_i = 0 \text{ on } \partial\Omega. \tag{B.12}$$

We solve Eqns. B.9 and B.10 weakly follow a standard finite element discretization and calculation procedure, using the alternating minimization (or staggered) scheme that runs parallel on high-performance computer clusters. We use the mechanical properties $E = 66.9$ GPa, $K_{\mathrm{IC}} = 1.53\,\mathrm{MPa\,m^{1/2}}$, and $\nu = 0.29$ in our PF simulations. The notched beam in the simulation shares the same geometry as the experiment specimen, having a notch of 250 µm in width and 1 mm in length. Since ℓ affects crack nucleation, it will affect values of w_x and w_y. Essentially, a smaller value of ℓ suggests more delayed crack nucleation, leading to larger values of w_x and w_y because of a larger stress build-up before crack nucleation. We find $\ell = 0.035$ mm to be a reasonable choice, and the corresponding results are presented in the main text. We pick an element size of $\delta h = 0.015$ mm near the crack propagation region, which is small enough ($\delta h \leq \ell/2$ [41]) to resolve the crack geometry. However, we emphasize that ℓ does not change the spatial pattern of w_x and w_y, which is a direct consequence of the balance of linear momentum. Figs. B.11(c) and B.12(c) shows results obtained from $\ell = 0.15$ mm. Compared to Figs. 6(c) and 7(c), the spatial pattern of $\bar{w}_x$ and $\bar{w}_y$ stays the same, but the magnitude is smaller.

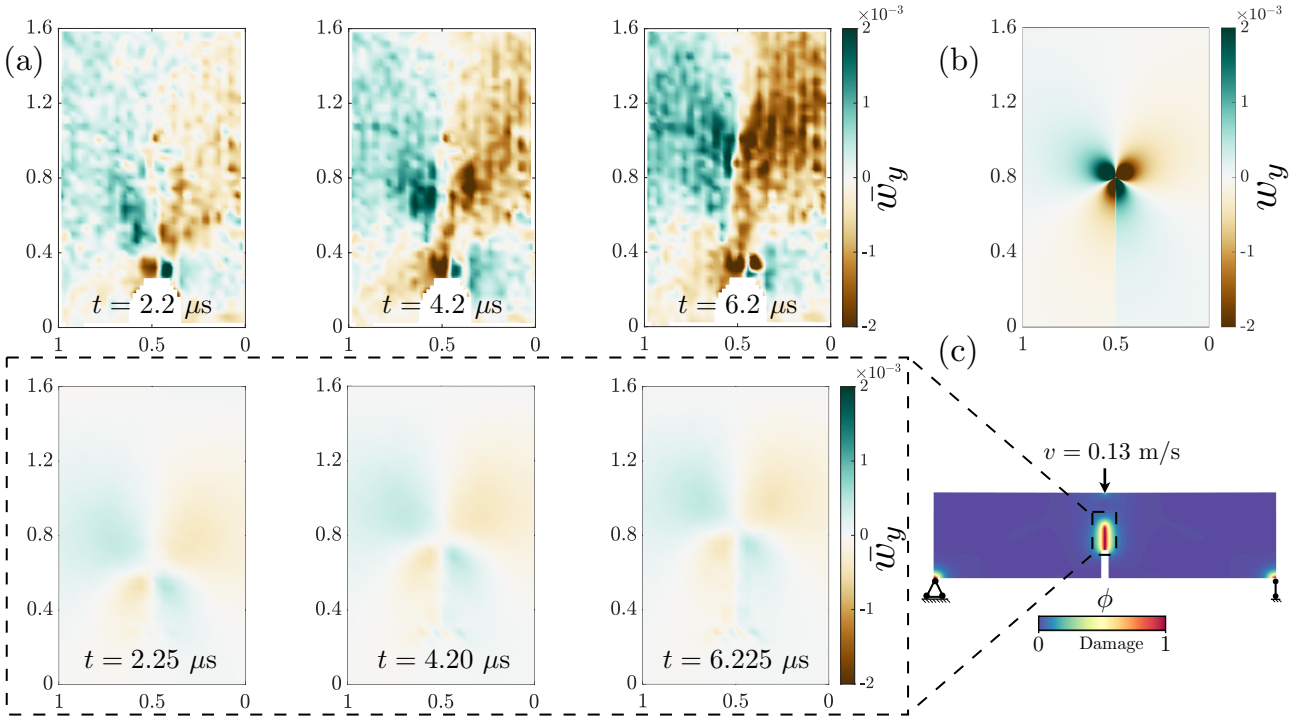

Figure B.11: A similar figure to Fig. 6 but with plots shown in (c) obtained from $\ell = 0.15$ mm.

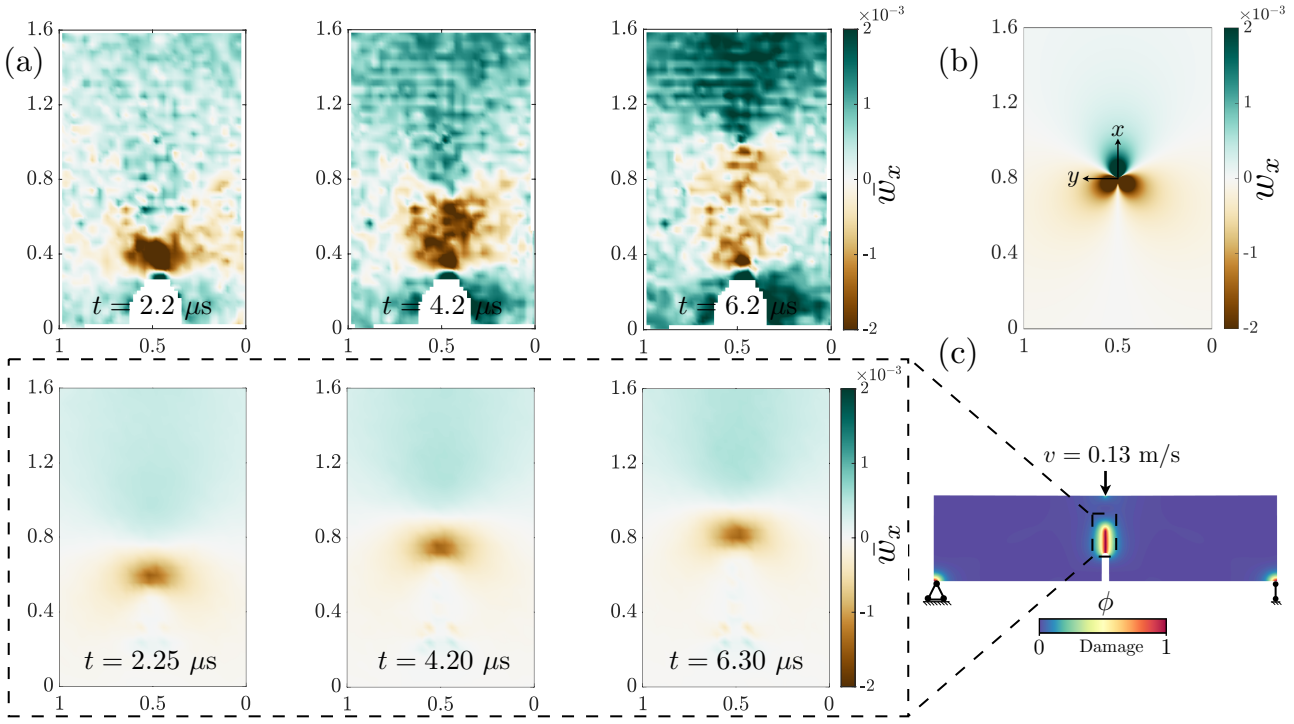

Figure B.12: A similar figure to Fig. 7 but with plots shown in (c) obtained from $\ell = 0.15$ mm.

Appendix C. Results of K_{I} using more terms

Fig. C.13 shows the result of K_{I} by including up to nine terms from Eqn. 4.5 in the fitting process. Indeed, the result is not sensitive to the number of terms considered.

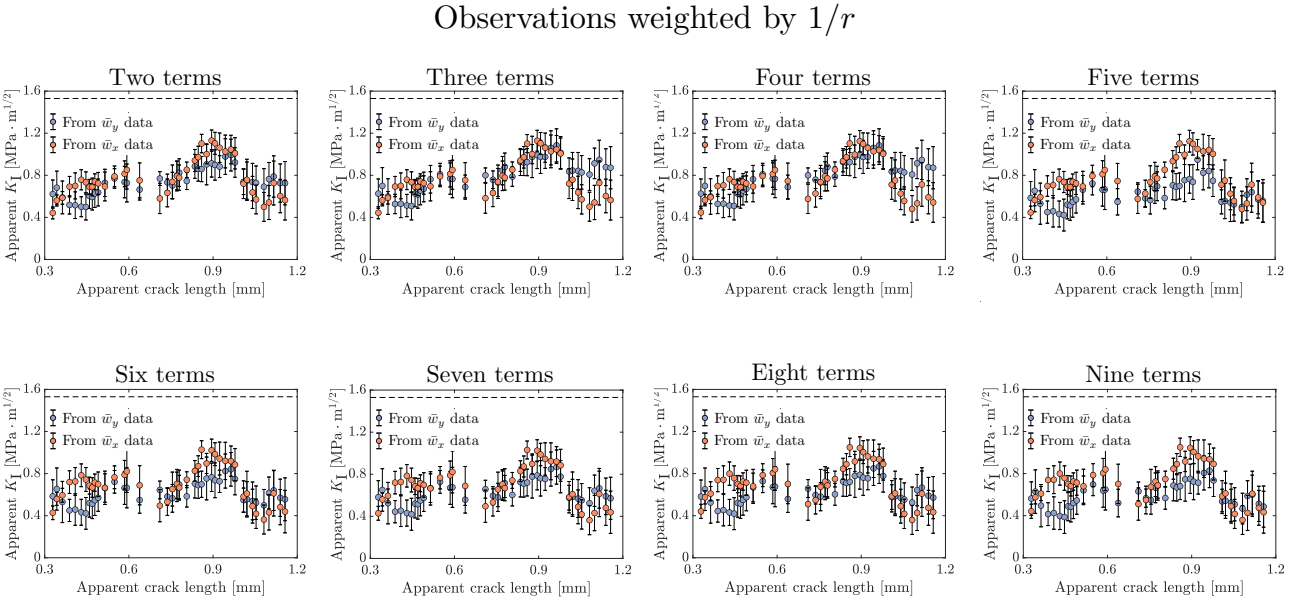

Figure C.13: Results of K_{I} variation as a function of the apparent crack length, using up to nine terms from Eqn. 4.5 in the fitting procedure based on Eqn. 4.9. The horizontal dash line in each figure corresponds to the static fracture toughness of Macor™.

Appendix D. 3D Abaqus/Explicit simulations

In the numerical model, we consider a standard three-point flexural test setup, which also mimicks our experimental loading condition. We consider a thin sample (h = 1.5 mm) and a thick sample (h = 0. 15 mm), each of which is supported by two cylinders on the bottom and loaded by one cylinder on the top. All objects (cylinders and samples) are discretized with standard tetrahedral elements that are locally refined near the crack tip region. Fig. D.14 shows the model. We consider cylinders to be made of steel and samples to be made of Macor™. Linear elasticity is used for both materials. Macor™ has a density of 2520 kg/m^3, a Young's modulus of 66.9 GPa, and a Poisson's ratio of 0.29. Steel has a density of 7830 kg/m^3, a Young's modulus of 210 GPa, and a Poisson's ratio of 0.3. General contact with a friction coefficient of 0.1 is used to characterize the contact behavior between cylinders and the samples. Fig. D.15 shows the in-plane stress gradient distribution calculated from the thin sample and the thick sample. Indeed, the former is similar to the latter, since the applied load scales with sample thickness. Fig. D.16 shows the distribution of σ_{zz} as a function of the distance to the crack tip. We observe that σ_{zz} decays much slower for the thick sample. In addition, the distance (r/h =0.5) at which σ_{zz} becomes negligible is also consistent with previous studies [44, 7].

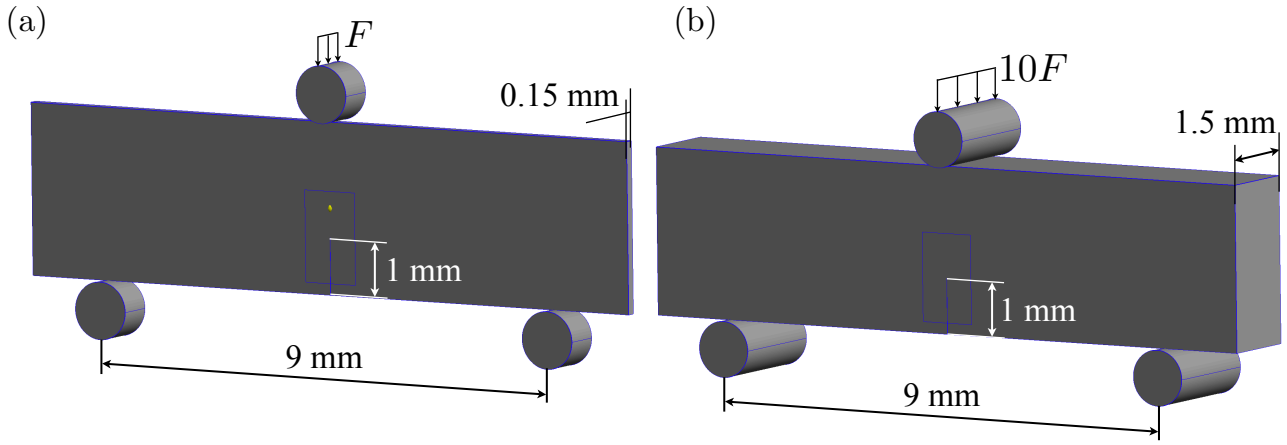

Figure D.14: Two numerical models constructed for Abaqus calculations: a thin sample (a) and a thick sample (b).

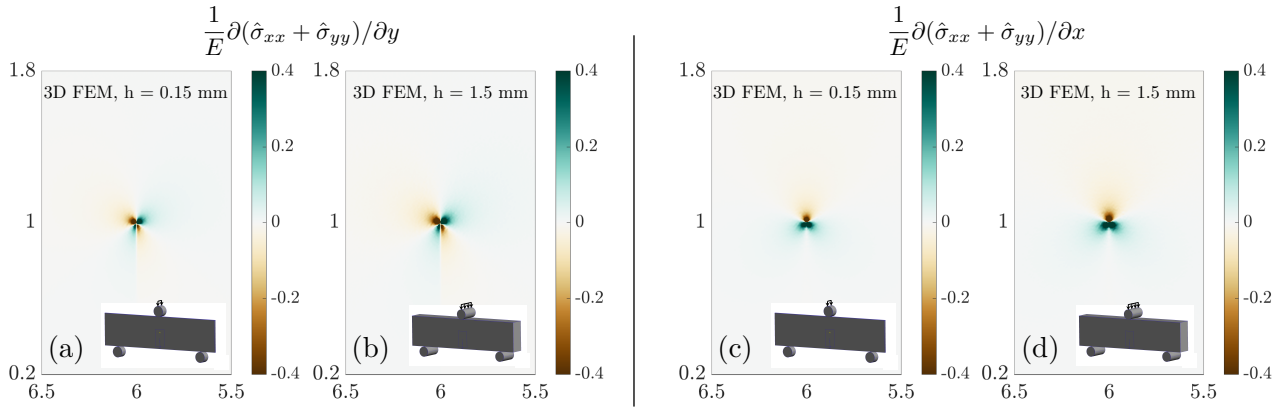

Figure D.15: Left column: Spatial distribution of $\partial(\hat{\sigma}_{xx}+\hat{\sigma}_{yy})/\partial y$ for the thin sample (a) and the thick sample (b). Right column: Spatial distribution of $\partial(\hat{\sigma}_{xx}+\hat{\sigma}_{yy})/\partial x$ for the thin sample (c) and the thick sample (d).

References

[1] James W Dally. Dynamic photoelastic studies of fracture: Dynamic photoelasticity is applied to characterize the behavior of cracks propagating in polymers and a metal with an -k relation. *Experimental Mechanics*, 19:349–361, 1979.

[2] K Ravi-Chandar. *An experimental investigation into the mechanics of dynamic fracture.* PhD thesis, California Institute of Technology, 1982.

[3] K Ravi Chandar and WG Knauss. Dynamic crack-tip stresses under stress wave loading—a comparison of theory and experiment. *International Journal of Fracture*, 20:209–222, 1982.

[4] AJ Rosakis, J Duffy, and LB Freund. The determination of dynamic fracture toughness of aisi 4340 steel by the shadow spot method. *Journal of the Mechanics and Physics of Solids*, 32(6):443–460, 1984.

[5] K-S Kim. A stress intensity factor tracer. 1985.

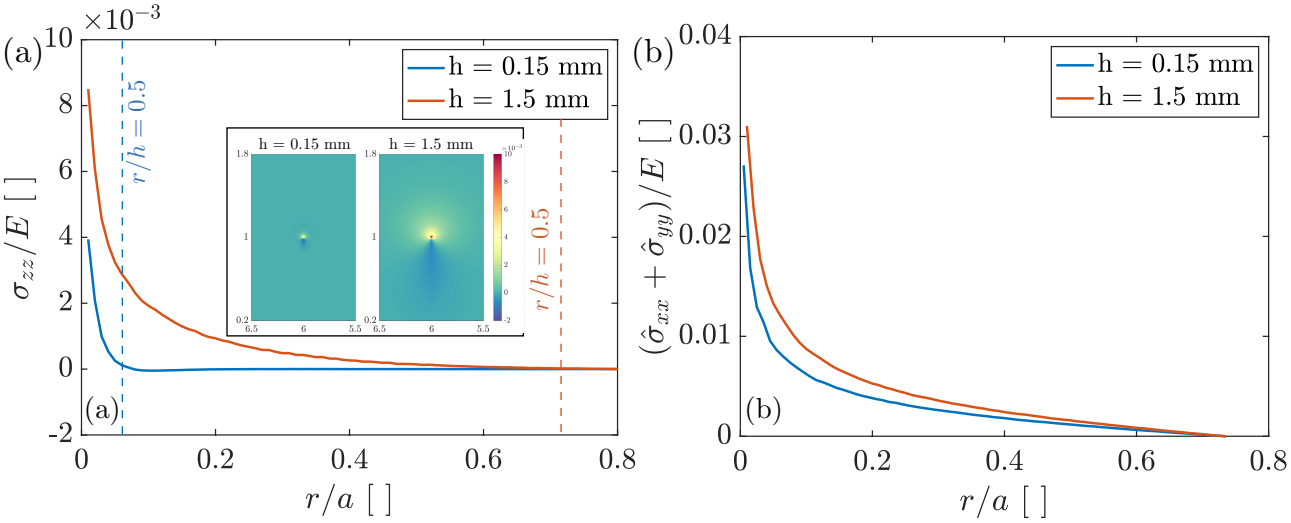

Figure D.16: (a) Distribution of the normalized out-of-plane stress σ_{zz}/E as a function of the normalized distance to the crack tip r/a for both the thin (blue) and the thick (red) sample, where a is the notch length equaling 1 mm. The inset figure visualizes the spatial distribution of σ_{zz} around the crack tip for the thin (left) and the thick sample (right). (b) A similar plot to (a) but for the distribution of the in-plane stress $(\hat{\sigma}_{xx} + \hat{\sigma}_{yy})/E$ for the thin (blue) and the thick (red) sample.

[6] Hareesh V Tippur, Sridhar Krishnaswamy, and Ares J Rosakis. A coherent gradient sensor for crack tip deformation measurements: analysis and experimental results. *International journal of fracture*, 48:193–204, 1991.

[7] Hareesh V Tippur, Sridhar Krishnaswamy, and Ares J Rosakis. Optical mapping of crack tip deformations using the methods of transmission and reflection coherent gradient sensing: a study of crack tip k-dominance. *International Journal of Fracture*, 52:91–117, 1991.

[8] Sridhar Krishnaswamy, Hareesh V Tippur, and Ares J Rosakis. Measurement of transient crack-tip deformation fields using the method of coherent gradient sensing. *Journal of the Mechanics and Physics of Solids*, 40(2):339–372, 1992.

[9] RJ Butcher, C-E Rousseau, and HV Tippur. A functionally graded particulate composite: preparation, measurements and failure analysis. *Acta Materialia*, 47(1):259–268, 1998.

[10] Madhu S Kirugulige, Hareesh V Tippur, and Thomas S Denney. Measurement of transient deformations using digital image correlation method and high-speed photography: application to dynamic fracture. *Applied optics*, 46(22):5083–5096, 2007.

[11] Gabriele Albertini, Mathias Lebihain, François Hild, Laurent Ponson, and David S Kammer. Effective toughness of heterogeneous materials with rate-dependent fracture energy. *Physical Review Letters*, 127(3):035501, 2021.

[12] Stephane Avril, Alain Vautrin, and Yves Surrel. Grid method: application to the characterization of cracks. *Experimental mechanics*, 44:37–43, 2004.

[13] Michel Grediac, Frédéric Sur, and Benoît Blaysat. The grid method for in-plane displacement and strain measurement: A review and analysis. *Strain*, 52(3):205–243, 2016.

[14] Chandru Periasamy and Hareesh V Tippur. Full-field digital gradient sensing method for evaluating stress gradients in transparent solids. *Applied Optics*, 51(12):2088–2097, 2012.

[15] C Miao and HV Tippur. Higher sensitivity digital gradient sensing configurations for quantitative visualization of stress gradients in transparent solids. *Optics and Lasers in Engineering*, 108:54–67, 2018.

[16] Balamurugan M Sundaram and Hareesh V Tippur. Dynamic fracture of soda-lime glass: A full-field optical investigation of crack initiation, propagation and branching. *Journal of the Mechanics and Physics of Solids*, 120:132–153, 2018.

[17] Krishnaswa Ravi-Chandar and Wolfgang G Knauss. An experimental investigation into dynamic fracture: Iii. on steady-state crack propagation and crack branching. *International Journal of fracture*, 26:141–154, 1984.

[18] L Lamberson, V Eliasson, and AJ Rosakis. In situ optical investigations of hypervelocity impact induced dynamic fracture. *Experimental mechanics*, 52:161–170, 2012.

[19] Chandru Periasamy and Hareesh V Tippur. A full-field reflection-mode digital gradient sensing method for measuring orthogonal slopes and curvatures of thin structures. *Measurement Science and Technology*, 24(2):025202, 2013.

[20] S Dondeti and HV Tippur. A comparative study of dynamic fracture of soda-lime glass using photoelasticity, digital image correlation and digital gradient sensing techniques. *Experimental Mechanics*, 60:217–233, 2020.

[21] Balamurugan M Sundaram and Hareesh V Tippur. Dynamic mixed-mode fracture behaviors of pmma and polycarbonate. *Engineering Fracture Mechanics*, 176:186–212, 2017.

[22] S Dondeti and HV Tippur. Cascading crack bifurcations in soda-lime glass: Quantification of fracture mechanics-based precursors using digital gradient sensing. *International Journal of Solids and Structures*, 234:111252, 2022.

[23] Wenfeng Hao, Can Tang, Yanan Yuan, Xuefeng Yao, and Yinji Ma. Experimental study on the fiber pull-out of composites using digital gradient sensing technique. *Polymer Testing*, 41:239–244, 2015.

[24] Chengyun Miao and Hareesh V Tippur. Fracture behavior of carbon fiber reinforced polymer composites: an optical study of loading rate effects. *Engineering Fracture Mechanics*, 207:203–221, 2019.

[25] Chengyun Miao and Hareesh V Tippur. Reflection-mode digital gradient sensing method: measurement accuracy. *Optical Engineering*, 58(4):044101–044101, 2019.

[26] Chengyun Miao and Hareesh V Tippur. A simplified reflection-mode digital gradient sensing technique for measuring surface slopes, curvatures and topography. *Optics and Lasers in Engineering*, 124:105843, 2020.

[27] Roland V Shack. Production and use of a lenticular hartmann screen. In *Spring Meeting of Optical Society of America, 1971*, volume 656, 1971.

[28] Ben C Platt and Roland Shack. History and principles of shack-hartmann wavefront sensing, 2001.

[29] SN Luo, BJ Jensen, DE Hooks, K Fezzaa, KJ Ramos, JD Yeager, K Kwiatkowski, and T Shimada. Gas gun shock experiments with single-pulse x-ray phase contrast imaging and diffraction at the advanced photon source. *Review of Scientific Instruments*, 83(7), 2012.

[30] Niranjan D Parab, John T Black, Benjamin Claus, Matthew Hudspeth, Jianzhuo Sun, Kamel Fezzaa, and Weinong W Chen. Observation of crack propagation in glass using x-ray phase contrast imaging. *International Journal of Applied Glass Science*, 5(4):363–373, 2014.

[31] Andrew FT Leong, Andrew K Robinson, K Fezzaa, T Sun, N Sinclair, DT Casem, PK Lambert, CJ Hustedt, Nitin P Daphalapurkar, KT Ramesh, et al. Quantitative in situ studies of dynamic fracture in brittle solids using dynamic x-ray phase contrast imaging. *Experimental Mechanics*, 58:1423–1437, 2018.

[32] Lawrence E Schmutz. Hartmann sensing at adaptive optics associates. In *Electromechanical system interaction with optical design*, volume 779, pages 13–17. SPIE, 1987.

[33] Bing Pan, Huimin Xie, Zhaoyang Wang, Kemao Qian, and Zhiyong Wang. Study on subset size selection in digital image correlation for speckle patterns. *Optics express*, 16(10):7037–7048, 2008.

[34] Kim I Mortensen, L Stirling Churchman, James A Spudich, and Henrik Flyvbjerg. Optimized localization analysis for single-molecule tracking and super-resolution microscopy. *Nature methods*, 7(5):377–381, 2010.

[35] M Kang, W Li, AFT Leong, M Guan, K Fezzaa, JT Harris, KT Ramesh, and TC Hufnagel. Crack nucleation and growth during dynamic indentation of chemically-strengthened glass. *Extreme Mechanics Letters*, 38:100754, 2020.

[36] Sung-Hoon Baik, Seung-Kyu Park, Cheol-Jung Kim, and Byungheon Cha. A center detection algorithm for shack–hartmann wavefront sensor. *Optics & Laser Technology*, 39(2):262–267, 2007.

[37] Max L Williams. On the stress distribution at the base of a stationary crack. 1957.

[38] Lambert Ben Freund. *Dynamic fracture mechanics*. Cambridge university press, 1998.

[39] Ilya Svetlizky and Jay Fineberg. Classical shear cracks drive the onset of dry frictional motion. *Nature*, 509(7499):205–208, 2014.

[40] pgo brochure. MACOR Machinable Glass Ceramic MGC. https://www.pgo-online.com/intl/macor-machinable-glass-ceramic.html, 2023. [Last update: 10.11.2023].

[41] Christian Miehe, Martina Hofacker, and Fabian Welschinger. A phase field model for rate-independent crack propagation: Robust algorithmic implementation based on operator splits. *Computer Methods in Applied Mechanics and Engineering*, 199(45-48):2765–2778, 2010.

[42] Michael J Borden, Clemens V Verhoosel, Michael A Scott, Thomas JR Hughes, and Chad M Landis. A phase-field description of dynamic brittle fracture. *Computer Methods in Applied Mechanics and Engineering*, 217:77–95, 2012.

[43] Liuchi Li, Jack Rao, Todd Hufnagel, and KT Ramesh. Meso-scale size effects of material heterogeneities on crack propagation in brittle solids. *arXiv preprint arXiv:2309.12916*, 2023.

[44] Ares J Rosakis and K Ravi-Chandar. On crack-tip stress state: an experimental evaluation of three-dimensional effects. *International Journal of Solids and Structures*, 22(2):121–134, 1986.

[45] AS Kobayashi and S Mall. Dynamic fracture toughness of homalite-100: Dynamic fracture toughness of homalite-100 determined by t. kobayashi and dally, as well as those of araldite b by kalthoff, beinert and winkler, are compared with those of the authors' previous results. errors generated through the use of static near-field crack-tip stresses for evaluating dynamic stress-intensity factor are also discussed. *Experimental Mechanics*, 18:11–18, 1978.

[46] Sh Akhondzadeh, Minju Kang, Ryan B Sills, KT Ramesh, and Wei Cai. Direct comparison between experiments and dislocation dynamics simulations of high rate deformation of single crystal copper. *Acta Materialia*, 250:118851, 2023.

[47] A Taylor Owens and HV Tippur. An image processing technique to identify crack tip position and automate fracture parameter extraction using dic: Application to dynamic fracture. *Experimental Mechanics*, 63(3):445–466, 2023.

[48] Swati Gupta, Grant West, Mark A Wilson, Scott J Grutzik, and Derek H Warner. Identifying crack tip position and stress intensity factors from displacement data. *International Journal of Fracture*, pages 1–17, 2023.

[49] Marco Endrizzi. X-ray phase-contrast imaging. *Nuclear instruments and methods in physics research section A: Accelerators, spectrometers, detectors and associated equipment*, 878:88–98, 2018.

[50] Liuchi Li and José E Andrade. Identifying spatial transitions in heterogenous granular flow. *Granular Matter*, 22(2):52, 2020.

[51] Blaise Bourdin, Gilles A Francfort, and Jean-Jacques Marigo. The variational approach to fracture. *Journal of elasticity*, 91:5–148, 2008.

[52] Alan Arnold Griffith. Vi. the phenomena of rupture and flow in solids. *Philosophical transactions of the royal society of london. Series A, containing papers of a mathematical or physical character*, 221(582-593):163–198, 1921.